ORIGINAL RESEARCH

Functional description of fiber orientation in paperboard based on orientation tensors resulting from μ-CT scans

**Greta Kloppenburg · Xiangfeng Li ·
Albrecht Dinkelmann · Hermann Finckh ·
Johannes Neumann · Jaan-Willem Simon**

Abstract Modern μ-CT scans offer non-destructive three-dimensional microstructure analysis of various materials. Despite small density contrasts, this technology also accurately captures the complex network structure of paper and paperboard. It provides detailed insight into the fiber orientation distribution in paper, which was previously unattainable with existing measurement methods. The image analysis results are applicable for numerical fiber network models, and simulations based on these models can significantly improve our understanding of the microstructural influence on macrostructural paper properties, such as strength, stiffness, and curl tendency. This work presents a new method for investigating the microstructural fiber orientation in paperboard. Orientation tensors obtained from μ-CT scan image processing are extracted and evaluated. Based on the direction of the orientation tensor's first eigenvector, the fiber orientation distribution is determined and then approximated by periodic and non-periodic probability density functions (PDFs). In this study, 40 commercial paperboard samples, each consisting of three plies, were analyzed. From a given set of commonly used PDFs, the best fitting ones have been identified based on their original location in the paper roll and on their ply. It was found that the von Mises PDF provided the most accurate representation of fiber orientation distribution in the middle ply, while the Elliptical PDF was the most suitable for the outer plies. Moreover, a more pronounced fiber orientation anisotropy was observed at the edges of the paper roll than in its center. The best PDFs and their function parameters are provided to allow for direct usage in numerical microstructure models of paperboard, thus enhancing their representativeness.

Keywords μ-CT scanning · Fiber orientation distribution · Orientation tensor · Periodic probability density functions · Paperboard

Introduction

Due to their renewable origin, cellulose-based materials appear to be a promising basis for rethinking and replacing carbon-based products. Research is currently being conducted on new materials such as (nano)cellulose foams (Motloung et al 2019) or cellulose fiber-reinforced composites (Miao and Hamad 2013).

However, cellulose-based materials are nowadays still primarily used in the form of paper and paperboard. These materials consist mainly of cellulose

G. Kloppenburg (✉) · X. Li · J. Neumann · J.-W. Simon
Computational Applied Mechanics, University
of Wuppertal, Pauluskirchstraße 7, 42285 Wupppertal,
Germany
e-mail: kloppenburg@uni-wuppertal.de

A. Dinkelmann · H. Finckh
German Institutes of Textile and Fiber Research,
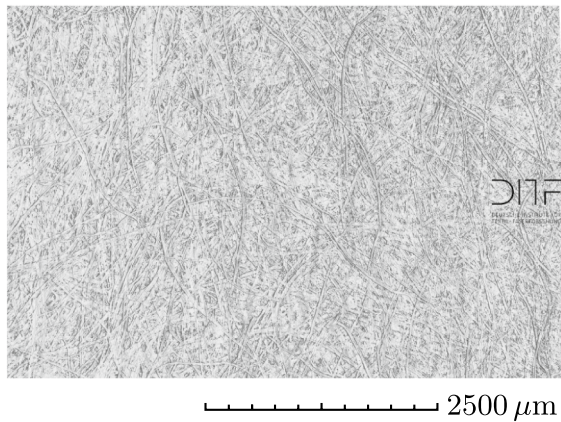Körschtalstraße 26, 73770 Denkendorf, Germany

Fig. 1 μ-CT scan image of an analyzed paperboard sample

fibers, which already have high variances in geometry and mechanical properties. The manufacturing process takes those heterogeneous fibers and introduces additional local differences to paper properties, such as density, thickness, or porosity (Niskanen 2008), resulting in a heterogeneous network structure, as can be seen in Fig. 1. Additionally, shear fields and accelerating flow (Wahlström 2009; Martin et al 2015) in the papermaking machine cause a pronounced orientation of the fibers in the machine direction. This leads to a globally anisotropic structural behavior. To understand this structural complexity on different scales and incorporate it into the improvement process of paper and paperboard, numerical modeling based on experimental studies is key. Recent research on multi-scale modeling of paper is summarized in (Simon 2021).

To develop realistic models of paper at the micro- or macroscale, the inclusion of single fiber orientation or global anisotropy is important as it influences various properties of paper and paperboard. These are: (i) in-plane paper mechanics, such as tensile strain and fracture properties (Lahti et al 2020; Johansson et al 2021), tensile stiffness and strength (Niskanen 2008; Wahlström 2013), tensile energy absorption (Wahlström 2013) and compressive strength (Niskanen 2008) (ii) structural deformations such as curl (Niskanen and Sadowski 1989; Kulachenko et al 2007; Decker et al 2013), cockling (Leppänen 2007; Lipponen et al 2008), and hygroexpansion (Uesaka 1994; Lavrykov et al 2004; Bosco et al 2015a; Lindner 2017) (iii) printing properties such as ink-paper

interaction (de Oliveira Mendes et al 2013). In order to determine a change in the properties mentioned, the change in fiber orientation or anisotropy must be statistically significant in each case. As an example, Wahlström (2009) and Benítez and Walther (2017) show that the stiffness increases with increasing fiber orientation in the direction of loading.

Over the decades, various experimental methods for measuring fiber orientation have been developed. For a recent overview, Dias et al (2023) is recommended. There, the methods are divided into direct and indirect methods (Niskanen and Sadowski 1989; Titus 1994). Methods in which individual (dyed) fibers and their orientation are identified are categorized as "direct" methods. In "indirect" methods, the measurement results from mechanical, acoustic, or radiation impacts are strongly influenced by the microstructural fiber orientation distribution. Therefore, this distribution can be derived from the results. Figure 2 shows a possible fiber distribution in polar form. In direct methods, discrete orientation angles are determined, which result in the sketched distribution. If indirect methods are applied, two parameters are detected: (i) the fiber anisotropy (ratio of the semiaxis a and b) and (ii) the preferential orientation angle (here denoted as γ), which indicates the deviation from the machine direction.

Some direct methods are limited to fiber detection on the paper surface. In (Marulier et al 2015; Orgéas et al 2021), dyed fibers are identified on the surface and the in-plane angular distribution for the fiber segments is determined. Dias et al (2023) uses a digital camera in combination with an illumination system to capture the surface structure and calculates the fiber orientation distribution based on the intensity gradients of the grayscale image. In (Enomae et al

Fig. 2 Sketch of a fiber orientation distribution that deviates from the machine direction (MD) by the preferential orientation angle γ. The ratio of the major and minor axes a and b indicates the structural anisotropy
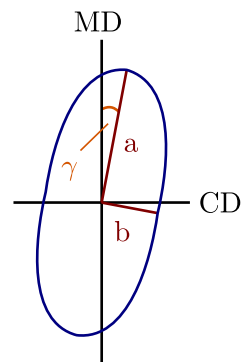
2006), two approaches for extracting the fiber orientation on the paper surface are presented, one using digital microscopy and one using scanning electron microscopy.

With the sheet splitting method, the fiber orientation and its change over the paper thickness can be tracked. The paper is split up into (up to) 200 layers (Hirn and Bauer 2007). The image data of each layer is captured using a microscope or scanner and analyzed through fiber segmentation or evaluation of gradient fields. The method is still up-to-date and was recently applied in (Wahlström 2009; Lahti et al 2020; Alzweighi et al 2021). It has good accuracy and repeatability, but is time-consuming (Hirn and Bauer 2007) and laborious (Niskanen 2008). Furthermore, this method is destructive, which limits the analysis possibilities. It is also not capable of evaluating the out-of-plane pointing fiber parts.

Another approach to directly determine the 3D fiber orientation is X-ray micro-computed tomography (μ-CT), where the 3D volume image is reconstructed from layer-wise data. There are various analysis methods for determining fiber orientation. In (Marulier et al 2012, 2015; Orgéas et al 2021), the fiber centerlines are captured manually and the in-plane and out-of-plane angle of the centerline segments are determined. Automated fiber detection is presented in (Viguié et al 2013), where fibers and fiber-fiber contact areas are identified by evaluating the orientation gradients. Based on the structure tensor of each voxel, the orientation of the fibers can be calculated without identification of each individual fiber (Axelsson 2008; Johansson et al 2021). In (Wallmeier et al 2021) the local orientation vector field is used to determine the in-plane orientation and the out-of-plane deviation of the fibers. The resolution of the method is in the micrometer range, and the possibility to examine the microstructure in three dimensions is not given by any of the other methods presented here. Moreover, further structural properties such as porosity (Rolland du Roscoat et al 2007; Charfeddine et al 2019; Neumann et al 2021), number of contact points and the fiber bond area (Urstöger et al 2020) as well as the presence of fillers (Rolland du Roscoat et al 2012) can be quantified from the μ-CT scans.

An indirect approach is ultrasonic testing, in which the fiber anisotropy is calculated by the ratio between the highest measured sound velocity and the velocity in the cross direction (Niskanen and Sadowski 1989; Enomae et al 2006; Schaffrath and Tillmann 2013). Similarly, the ratio of the elastic modulus in the machine and cross directions, which is obtained from uniaxial tensile tests, provides information about the fiber anisotropy (Niskanen and Sadowski 1989; Nygårds 2022). Both methods are established in the paper industry (Hess and Brodeur 1996). However, since the paper stiffness depends not only on the fiber orientation, but also on internal drying stresses, the determined fiber orientation can deviate from the actual one (Hess and Brodeur 1996).

In optical methods, fiber anisotropy is determined indirectly by evaluating the patterns of transmitted or diffracted radiation through the paper. X-rays are diffracted by the crystalline regions of the fibers. Based on the intensity of the scattered radiation, conclusions can be drawn about the fiber anisotropy in the paper (Niskanen and Sadowski 1989). When laser beams are directed at the paper, the direction and intensity of the main fiber orientation direction can be determined by the elliptical pattern of the transmitted (Niskanen and Sadowski 1989; Mendes et al 2015) or diffracted (Niskanen and Sadowski 1990; Fiadeiro et al 2002) light. These methods are, except for the laser diffraction technique (Niskanen 2008), non-destructive and independent of internal stresses, but evaluate rather small areas (Niskanen and Sadowski 1989).

When using the μ-CT method, image analysis approaches can be based on the detection of individual fibers. For a heterogeneous material such as paper with irregularly shaped and bonded fibers, automatic fiber detection is not yet fully developed, so that the fibers are still detected manually in some studies (Marulier et al 2012, 2015; Orgéas et al 2021). This is very costly and time-consuming. Another approach to image analysis is to evaluate grayscale gradients in each voxel to determine its orientation state. This orientation state can be expressed by second-order orientation tensors (Bauer and Böhlke 2021), which are based on the fundamental works of Kanatani (1984) and Advani and Tucker (1987). By spectral decomposition of the orientation tensor, the structural features are separated from its spatial alignment (Bauer et al 2023) and can be directly interpreted physically (Köbler et al 2018). In addition, fourth-order orientation tensors, which are used for instance in mechanical models to estimate the elastic stiffness (Orgéas et al 2021), can be generated from second-order

tensors by closure approximations (Breuer et al 2019; Görthofer et al 2020; Bauer and Böhlke 2021).

The fiber orientation distributions measured with previously presented methods can be approximated by probability density functions (PDFs). In the fundamental work of Perkins and Mark (1981), the Cosine PDF, the von Mises PDF and the Elliptical PDF were proposed for this purpose. Further function types and comprehensive overviews can be found in (Sampson 2001; Wahlström 2009). The PDFs are used, for example, in the generation step of numerical fiber network models to assign an in-plane orientation to the fibers. In recent works, the following functions are used: Non-periodic Gaussian distributions (Brandberg et al 2020; Lin et al 2021), periodic Cosine distributions (Bronkhorst 2003; Görtz et al 2022) as well as the periodic Cauchy distribution (Bosco et al 2015b) and the periodic Elliptical distribution (Ceccato et al 2021), which can be transformed into each other (Wahlström 2009).

In this work, a new method for describing fiber orientation in paperboard with non-periodic and periodic probability density functions is presented. The μ-CT scanning technique is chosen to capture the paperboard microstructure. It offers the possibility to analyze the fiber orientation change across the thickness without destroying the material and allows an efficient examination of a large number of samples. Here, μ-CT scans of 40 paperboard samples are performed and analyzed by a voxel-based evaluation using second-order orientation tensors. Spectral decomposition of the orientation tensors reveals the principal orientation directions. These directions are expressed in the form of spherical coordinates and their distribution is calculated to search for the most suitable PDF type for describing the fiber distribution. Based on this method, the fiber orientation analysis is twofold: (i) location wise, (ii) ply-wise. Firstly, it

is analyzed without differentiating between the three paperboard plies, but depending on their initial location on the paper roll. Secondly, the plies are analyzed separately to quantify structural differences between them and to find the best PDF for each ply. In addition to the PDF types, their functional parameters are given to support the development and improvement of numerical microstructure models such as presented in (Li et al 2018; Kloppenburg et al 2023b).

Material

Commercial three-ply paperboard used for packaging was examined. A total of 40 samples were analyzed. They differed only in their original position on the paperboard roll (hereafter abbreviated as paper roll), while the board type was identical across all samples. Half of them was taken from the paper roll edge and the other half from the paper roll center. Figure 3 illustrates the sample collection procedure. From five paper rolls (later labeled with the letters A to E), one sheet of paperboard was taken from the edge and center. Afterward, four samples were cut out of each sheet by laser cutting and then scanned using μ-CT scanning.

The paperboard had a grammage of 240 g/m^2 and a total average thickness of 386 μm. It was composed of three plies with differing thickness and fiber types as shown in Fig. 4. This layered structure with a bulky core and with dense and stiff surface plies guaranties high bending stiffness while minimum grammage (Fellers et al 2001; Niskanen 2008). The top ply was 100 μm thick and it consisted of bleached chemical softwood pulp fibers. In the middle, a mix of chemo-thermo-mechanical pulp fibers, chemical softwood fibers and broke was used. With 200 μm it was the thickest ply. The thinnest ply was the bottom ply with

Fig. 3 Sheets were taken from the center and edge of a paper roll (**a**) and the test samples were cut out of the sheets (**b**). The asymmetric sample shape with the area of the high resolution scan is shown in (**c**)
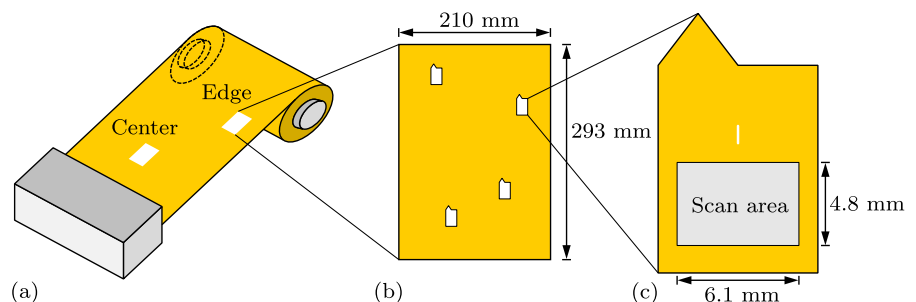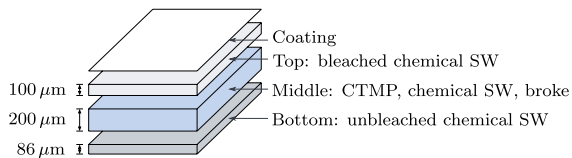
Fig. 4 Paperboard structure with ply thicknesses and fiber mix (softwood (SW), chemo-thermo-mechanical pulp (CTMP))

Fig. 5 Overview scan area covering the entire sample and smaller detail scan area with a slight tilt to the set evaluation grid

86 µm. It consisted of unbleached chemical softwood pulp fibers. At the end of the paperboard manufacturing process, a coating was applied on the outer side of the top ply to guarantee good printability.

Image acquisition

The image acquisition included the preparation and execution of the X-ray µ-CT scans as well as the translation of the images into discrete fiber network orientation and density information.

µ-CT scanning generally is a non-destructive imaging method. For optimum image quality, however, it was necessary to rotate the test specimen by 360° during the scan, which meant that the test specimen had to be appropriately small, as it could only be a few millimeters away from the X-ray source. For this reason, it was necessary to cut samples out of the sheet using a *trotec speedy 100* laser cutter. As depicted in Fig. 3, the samples had an asymmetric shape consisting of a rectangle and a triangle at the rectangle's top edge. This allowed reliable differentiation between the front and back of the sample. Furthermore, a one-millimeter cut was made above the scan area to serve as a reference.

For the µ-CT scanning, a *Phoenix Nanotom M* from Waygate Technologies was used. Since paper, consisting of cellulose fibers and air voids, has a lower density than metal, for example, the voltage and current of the X-ray tube had to be appropriately chosen. To get a high absorption signal despite the low density of paper, the accelerating voltage was reduced to 80 kV compared to the maximum possible voltage of 180 kV. The amount of current applied to the filament in the X-ray tube was a tradeoff between light yield and target focus on the sample. A current of 220 µA was chosen as a compromise. With this parameter, the focal spot diameter corresponded to a magnification of 50 in the detail scan.
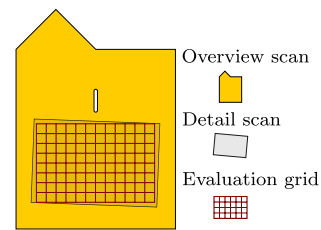
A challenge in performing µ-CT scans was to avoid blurring effects in the resulting images. On the one hand, a thermal shift can occur due to changing temperatures or moisture contents. On the other hand, the clamping can cause a mechanical shift. Both were prevented by storing and stabilizing the clamped samples for several hours in a thermally stable chamber at room temperature and humidity. Before starting the scanning process, it was necessary to check whether the X-ray source, the specimen axis and the center of the detector were aligned, since a deviation can lead to a lower image quality. Furthermore, a shift in the focal point due to the impact of the electron beam on the X-ray target can also lead to a blurred image. To correct this, a scan with 18 images was performed before the actual main scan was started. During the main scan, the sample was rotated by 360° in 4000 steps. Four images were acquired at each position with a respective exposure time of half a second. In the reconstruction, the first image of each position was skipped to avoid inaccuracies due to the oscillation of the sample after stopping the rotation. An average value was then calculated from the remaining three images. For the reconstruction *datos 2|rec* from GE Measurement & Control with 32bit gray value calculation was used.

At first, an overview scan over the entire sample area with a resolution of 5 µm voxel edge length (focus to detector distance (FDD) 600 mm; focus to object distance (FOD) 30 mm; magnification 20) was recorded. This was done in order to align the detail scan images by adjusting them to the overview scan, because they sometimes had a small offset in the form of a tilt relative to the sample edges as depicted in Fig. 5. The scanning resolution of the high resolution detail scan was 2 µm voxel edge length (FDD 600 mm; FOD 12 mm; magnification 50).

After scanning and reconstruction, the sample structure was analyzed using *VGSTUDIO MAX 3.0* from Volume Graphics Gmbh. Before determining the fiber volume fraction and fiber orientation, the direction of the scanned area was adjusted. As previously mentioned, the detail scan was slightly tilted with respect to the sample edges. To avoid bias in the fiber direction, the detail scan was aligned with the overview scan so that the fibers of the detail scan overlapped with those of the overview scan. This slight tilt resulted in the evaluation area being a little smaller than the actual detail scan.

Subsequently, a threshold value for the distinction between matter and air had to be determined in order to be able to read physical information from the images. For this purpose, the histogram of the gray values across all voxels was generated and the midpoint between the two maxima of air and matter was defined as the threshold value.

To determine the fiber volume fraction of the microstructure, based on the intensity of the gray value of all voxels of the scanned volume a distinction was made between fiber material (light gray value) and air (dark gray value). In this way, not only pores but also the lumen of non-collapsed fibers could be detected as air. The gray value of air voxels in the lumen or close to a fiber surface was often darker than the gray value of air voxels further away from the material due to the small-angle scattering of the X-rays. This had to be taken into account when differentiating between the two components, material and air.

For the determination of the fiber orientation, a gradient field was calculated from gray values of adjacent voxels and a direction was derived from this. Since all voxels, including the air voxels, would thus receive a direction, a threshold value had to be assigned to the gradient field on the basis of which air voxels could be detected.

Second-order orientation tensors were calculated for previously defined cells of a grid based on the directions of the voxels. Orientation tensors reflect the orientation information averaged over all voxels of the cell. As shown in Fig. 6, these cells had a size of 500 µm × 500 µm in the plane and a height of 2 µm, corresponding to 250 × 250 voxels. In the following, these cells will be referred to as "evaluation cells". In Fig. 7, the orientation tensors of the evaluation cells for a plane within the sample are
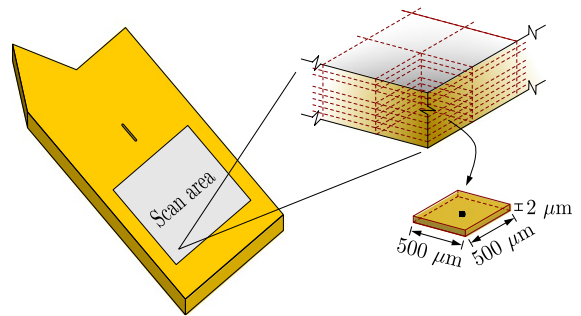

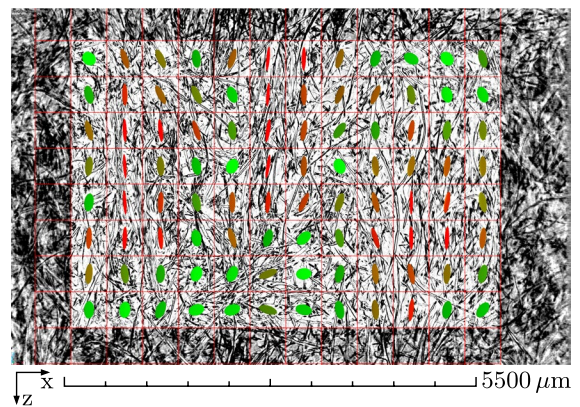**Fig. 6** Sketch of the grid used in postprocessing and an evaluation cell with its dimensions

Fig. 7 Virtual section in the plane (x-z-plane) at y = 227.89 µm (out-of-plane direction). The red lines represent the evaluation grid with the 500 µm × 500 µm cells. In some parts of this section, the fibers are uniformly distributed (green, wide ellipses) and in other parts, a strong anisotropy is present (red, needle-like ellipses)

shown as ellipses. In the case of a rather isotropic distribution of fibers in an evaluation cell, the ellipse is nearly circular and shown in light green. If there is a pronounced preferred fiber direction, the shape of the ellipse resembles a pin and is colored dark red. It should be noted that the orientation tensor generally contains not only in-plane but also out-of-plane direction components and should, therefore, be considered as an ellipsoid. This will be explained in more detail in Section Orientation tensor.

The final outcome of the image acquisition are information about the coordinates of the evaluation cells, their orientation tensors and fiber volume fractions, and the number of voxels analyzed in them. Since the size

of the detail scan was 6.1 mm × 4.8 mm with a height of about 400 μm, more than 20,000 evaluation cells were analyzed in terms of their fiber orientation and fiber volume fraction. This was done for the 40 samples, as described in Section Material.

Statistical methods

In the following, it is shown how orientation angles were calculated from the orientation tensors and how the distribution of these could be described using probability density functions.

Orientation tensor

The mean fiber orientations determined from the μ-CT scans were described using second-order orientation tensors. An orientation tensor $\mathbf{A}$ of Kanatani's first kind (Kanatani 1984) is defined by Advani and Tucker (1987) as

$$\mathbf{A} = \oint \Psi(\mathbf{p})\, \mathbf{p} \otimes \mathbf{p}\, \mathrm{d}\mathbf{p}. \tag{1}$$

In this, $\Psi(\mathbf{p})$ corresponds to the fiber orientation density function, $\mathbf{p}$ with $\|\mathbf{p}\| = 1$ to the unit vector of the fiber axis orientation, and $\oint \mathrm{d}\mathbf{p}$ to the integral over the unit circle. The formulation can be understood as a weighted summation of the different orientations (Bauer and Böhlke 2021), where the moment tensor $\mathbf{p} \otimes \mathbf{p}$ describes a particular direction in tensorial form, and the fiber orientation density function $\Psi(\mathbf{p})$ serves as the weighting factor of that direction.

The fiber orientation density function $\Psi(\mathbf{p})$ must fulfill certain conditions. The function has to be non-negative

$$\Psi(\mathbf{p}) \geq 0. \tag{2}$$

It must be symmetric, since the fiber direction is bidirectional

$$\Psi(-\mathbf{p}) = \Psi(\mathbf{p}). \tag{3}$$

Furthermore, the orientation density function must be normalized so that

$$\oint \Psi(\mathbf{p})\, \mathrm{d}\mathbf{p} = 1 \tag{4}$$

holds. The Kanatani's first kind orientation tensor (Kanatani 1984) is symmetric and positive-definite. This is evident from relations (1) and (2). Thus, $\mathbf{A}$ can be diagonalized. For a more detailed explanation of the properties and the variety of orientation tensors, the work of Bauer and Böhlke (2021) is recommended.

The diagonalization transforms the orientation tensor from the fixed basis system $\{\mathbf{e}_i\}$ into the eigensystem $\{\mathbf{v}_i\}$, which is spanned by the eigenvectors $\mathbf{v}_i$ with $i = 1, 2, 3$. The entries λ_i with $\lambda_i \geq 0$ of the corresponding diagonal matrix $\mathbf{A}$ are the eigenvalues. This is shown by the relation

$$\mathbf{A} = A_{ij}\, \mathbf{e}_i \otimes \mathbf{e}_j = \sum_{i=1}^{3} \lambda_i\, \mathbf{v}_i \otimes \mathbf{v}_i = \begin{bmatrix} \lambda_1 & 0 & 0 \\ & \lambda_2 & 0 \\ \mathrm{sym} & & \lambda_3 \end{bmatrix} \mathbf{v}_i \otimes \mathbf{v}_j. \tag{5}$$

As often found in the literature, the eigenvalues are ordered by their magnitude

$$\lambda_1 \geq \lambda_2 \geq \lambda_3. \tag{6}$$

Furthermore, it holds that

$$\lambda_1 + \lambda_2 + \lambda_3 = 1. \tag{7}$$

This is equivalent to $\mathrm{tr}(\mathbf{A}) = 1$, which is a consequence of the normalization of the fiber orientation density function (4) and the normalized orientation vectors $\mathbf{p}$ with $\|\mathbf{p}\| = 1$.

Transforming the orientation tensor into its eigensystem allows a straightforward physical interpretation of the fiber orientation state. The eigenvectors $\mathbf{v}_i$ with $i = 1, 2, 3$ represent the three principal fiber directions, and the probability of finding fibers in that direction is given by the eigenvalues λ_i (Köbler et al 2018).

This can be illustrated using an ellipsoid, as shown in Fig. 8a. The eigenvectors, scaled by their eigenvalues, span the ellipsoid as semi-axes (Cowin 1985; Bauer and Böhlke 2021). Thus, the shape of the ellipsoid can be used to assess the investigated orientation state. If the orientation state is isotropic ($\lambda_1 = \lambda_2 = \lambda_3 = \frac{1}{3}$), the ellipsoid appears spherical. On the other hand, if there is significant anisotropy in one direction ($\lambda_1 \gg \lambda_2 > \lambda_3$), then the ellipsoid takes a needle-like form. According to a planar orientation state ($\lambda_3 = 0$), the ellipsoid is reduced to a two-dimensional ellipse.
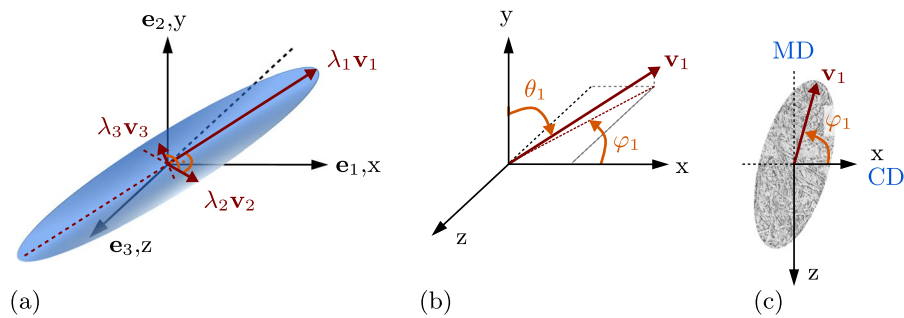
(a)

(b)

(c)

Fig. 8 a Ellipsoid representing an orientation tensor in its eigensystem with eigenvectors $\mathbf{v}_i$ scaled with their eigenvalues λ_i as semi-axes ($i = 1, 2, 3$). **b** In-plane angle φ_1 pointing from the x-axis to the first eigenvector $\mathbf{v}_1$ and out-of-plane angle θ_1 pointing from the y-axis to $\mathbf{v}_1$. **c** Connection between x,y,z-base system and the machine direction (MD) and cross direction (CD)

Orientation angles

For the functional description of the orientation state of the fibers in the microstructure, the first eigenvector $\mathbf{v}_1$ of the orientation tensors was used and the distribution of its direction was evaluated by the orientation angles θ_1 and φ_1, as shown in Fig. 8b. This approach implies that not all the information contained in an orientation tensor was used. For instance, the extent to which the first principal direction dominates over the other principal directions, as indicated by the eigenvalues, was initially disregarded.

The angle θ_i ($i = 1, 2, 3$), defined in the range from 0 to $\frac{\pi}{2}$, is located between the y-axis and the eigenvector $\mathbf{v}_i$. It indicates how much the eigenvector is inclined out of the plane, which is why it will be often referred to as the "out-of-plane angle" in the following. The angle φ_i ranging from 0 to π represents the angle between the x-axis and the in-plane projection of the eigenvector $\mathbf{v}_i$ and will be denoted as "in-plane angle". It should be noted that the y-axis is perpendicular to the plane, whereas the x- and z-axes span the plane here. The eigenvectors $\mathbf{v}_i$ are defined as position vectors in Euclidean space and describe a direction based on the connection of the origin to a point defined by the x-, y- and z-coordinates. In order to describe this direction using the spherical coordinates θ and φ, the transformations

$$\varphi_i = \begin{cases} \pi - \arctan\left(\frac{\mathbf{v}_{i,3}}{\mathbf{v}_{i,1}}\right), & \text{if } \operatorname{sign}(\mathbf{v}_{i,3}) = \operatorname{sign}(\mathbf{v}_{i,1}) \\ \left|\arctan\left(\frac{\mathbf{v}_{i,3}}{\mathbf{v}_{i,1}}\right)\right|, & \text{if } \operatorname{sign}(\mathbf{v}_{i,3}) \neq \operatorname{sign}(\mathbf{v}_{i,1}) \text{ and} \end{cases}$$

(8)

$$\theta_i = \arccos\left(\mathbf{v}_{i,2}\right) \tag{9}$$

were carried out. The index i with $i = 1, 2, 3$ represents the three eigenvectors $\mathbf{v}_i$ and the additional index numbers 1, 2 and 3 represent their x-, y- or z-coordinates.

The in-plane angle φ is essential in analyzing the microstructure of paper, as the fibers usually barely protrude out of the plane. Thus, Fig. 8c depicts the in-plane angle φ in two dimensions, with respect to the global coordinate system, and in relation to the machine direction (MD) and cross direction (CD). In the field of paper science, the in-plane angle is often defined between the machine direction and the preferential fiber direction, as shown in Fig. 2 denoted with γ. Based on this definition, the prevalent fiber orientation is around 0° there. However, since the x-axis here corresponds to the cross direction (CD), the largest proportion of fiber angles lies at about 90°.

Limitation to the in-plane orientation angle φ

In the subsequent sections, the analysis of the fiber orientation in the microstructure of multi-ply paperboard is limited to the in-plane orientation of the fibers. The validity of this approach is shown below.

To assess the portion of out of the plane protruding fiber parts and fibers, the direction of the three eigenvectors described by the out-of-plane angle θ_i and the three eigenvalues λ_i were analyzed. This combined consideration of eigenvectors and eigenvalues is necessary to comprehensively examine the microstructural orientation state (Müller et al 2015).

The out-of-plane angles and eigenvalues were derived from the orientation tensors of all samples, and their respective statistical distributions are depicted in Figs. 9 and 10 using boxplots.

In the boxplots, the red dot corresponds to the mean value of the data set, the horizontal line in the box indicates the median and the upper and lower edges of the box correspond to the 25th and 75th percentiles. The distance between the two edges is called the interquartile range (IQR). It defines the length of the whiskers, which is 1.5 IQR. However, if the distance between the minimum or maximum of the analyzed dataset and the edge of the box is less than 1.5 IQR, the whisker length is limited to that distance. Any values outside the 1.5 IQR range are identified as outliers and are marked with blue circles. For the purpose of clarity, they are not displayed in certain figures such as Figs. 9 and 10.

Figure 9 shows the distributions of the angles θ_i which point from the y-axis towards the three eigenvectors $\mathbf{v}_i$. The out-of-plane angle to the first and second eigenvectors is close to 90° corresponding to an in-plane orientation (x-z-plane in Fig. 8). The inclination of the third eigenvector to the y-axis is close to 0° or 180° which corresponds to an out-of-plane orientation perpendicular to the x-z-plane. The distributions of the eigenvalues of the three eigenvectors are displayed in Fig. 10. Clearly, λ_1 and λ_2 are considerably larger than λ_3. This means that the fiber portion that is represented by the first two eigenvectors lie in the plane, and that they form the majority of fibers
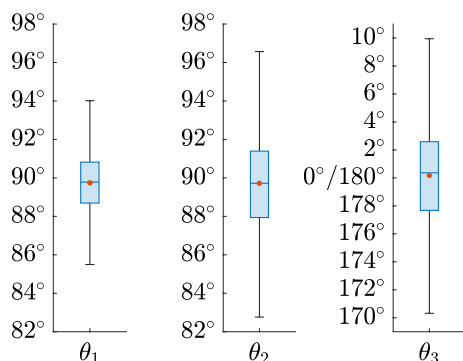

Fig. 10 Boxplot showing the distribution of eigenvalues λ_i ($i = 1, 2, 3$) of all 40 samples. The red dot represents the data mean and the line inside the box is the data median

due to their larger eigenvalues compared to λ_3. Therefore, the portion of fibers pointing out-of-the plane is negligibly small and an in-plane fiber orientation can be assumed.

This conclusion is further strengthened by the orientation triangle (Cintra and Tucker 1995; Chung and Kwon 2002; Köbler et al 2018) shown in Fig. 11. The points in the orientation triangle represent the eigenvalues λ_1 and λ_2 of the orientation tensors of all samples. In addition, the triangle contains information about the value of λ_3 through relationship (7). Depending on the location of a point in the orientation triangle, specific orientation states can be identified. The vertices A, B and C mark the three extremal orientation states isotropic ($^1/_3$, $^1/_3$), planar isotropic (0.5, 0.5) and unidirectional (1, 0). At the

Fig. 9 Boxplot showing the distribution of the out-of-plane angles θ_i ($i = 1, 2, 3$) of all 40 samples ($\sim 800\,000$ data points) pointing from the out-of-plane y-axis to the eigenvectors $\mathbf{v}_i$. The red dot represents the data mean and the line inside the box is the data median
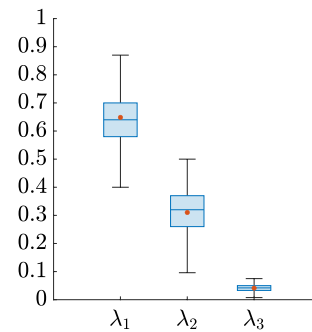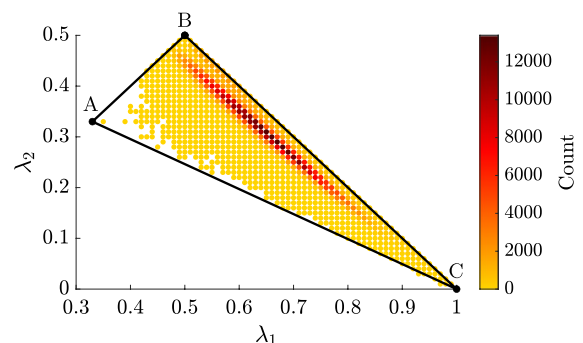

Fig. 11 Orientation triangle representing the eigenvalues of all 40 samples ($\sim 800\,000$ data points). The third eigenvalue is $\lambda_3 = 1 - \lambda_1 - \lambda_2$. The color of the points inside the triangle indicates how often the eigenvalue combination occurred. The vertices A, B and C correspond to an isotropic, planar isotropic and unidirectional orientation state, respectively

edge between the point A and B, λ_1 equals λ_2, which is equivalent to transversal isotropy with the preferred direction 3. The same applies to the connection of the points A and C, where λ_2 is equal to λ_3 and where again transversal isotropy with the preferred direction 1 is present. At the edge between the points B and C, λ_3 is always equal to zero, reflecting a planar orientation state. In general, all orientation states are either inside the triangle, corresponding to an orthotropic orientation state, or on the edges of the triangle. When referring to Fig. 11, the color scale shows the absolute occurrence of $\lambda_1 - \lambda_2$-combinations. It can be seen that the vast majority of combinations appear near the "planar" edge, where λ_3 equals zero. Knowing that the corresponding eigenvectors $\mathbf{v}_1$ and $\mathbf{v}_2$ lie mainly in the plane (see Fig. 9), this supports the assumption of a planar fiber distribution in the investigated microstructures of the considered paperboard.

Orientation distribution functions

As elucidated before, the current focus is on the investigation of fiber orientation in the plane. Figure 12 shows how a distribution of the in-plane orientation angles φ_1 of one of the tested samples looks like. For a more comprehensive analysis of in-plane fiber orientation, the choice of a suitable representation of the distributions is crucial. Since the resulting data of the histograms are always discrete and depend on bin size, the aim of this study is to provide a functional description of the distribution. This makes it possible to store the information
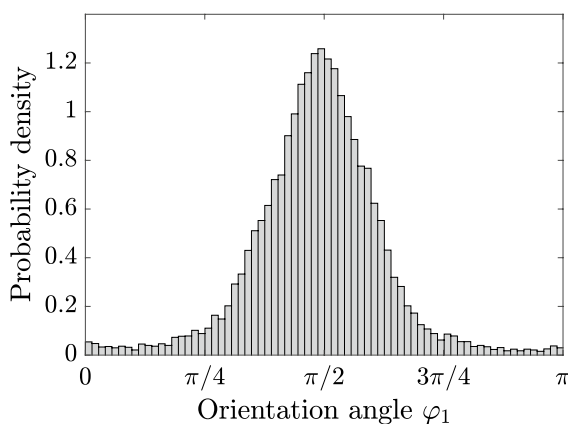

Fig. 12 Histogram of in-plane angle φ_1 distribution in an analyzed sample

of the distribution in condensed form, to analyze it immediately based on the function parameters, and to use it in numerical models. Established probability density functions (PDFs) were used for the functional description. They have only two or three characteristic function parameters that control the appearance of the function curve. The function parameters often have a physical meaning, so that a direct interpretation of the distribution is possible, for example via the location or dispersion parameter.

Here, the angular distributions were described using both non-periodic and periodic PDFs. The non-periodic functions provided a first start into the functional analysis, as can be read in (Kloppenburg et al 2023a). Compared to periodic PDFs, a large number of them have already been implemented in numerical calculation softwares and can therefore be used directly. Nevertheless, periodic functions are able to represent the periodic characteristic of the angular data, which is similar to the relation in (3). Moreover, the use of this type of function is already established in paper science. The equations of the non-periodic and periodic PDFs that were most suitable are listed in the following.

Non-periodic probability density functions

To investigate which non-periodic PDF best describes the distribution of the orientation angle in the plane, several functions integrated in MATLAB were tested. The functions listed below are the remaining non-periodic PDFs selected based on the goodness-of-fit test.

The **t-location scale PDF** is defined as

$$f(\alpha \mid \mu, \sigma, \nu) = \frac{\Gamma\left(\frac{\nu+1}{2}\right)}{\sigma\sqrt{\nu\pi}\,\Gamma\left(\frac{\nu}{2}\right)} \left[\frac{\nu + \left(\frac{\alpha-\mu}{\sigma}\right)^2}{\nu} \right]^{-\left(\frac{\nu+1}{2}\right)}.$$

(10)

The parameter $\Gamma(\cdot)$ represents the gamma function, and in all non-periodic PDFs μ is the location parameter, σ the scale parameter and ν the shape parameter. The effect of changing function parameter values is illustrated in Fig. 13.
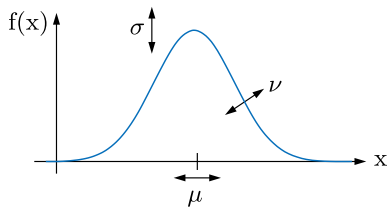
The **Logistic PDF** reads

Fig. 13 Effects of changing the values of the location parameters μ, the scale parameter σ and the shape parameter ν

$$f(\alpha \mid \mu, \sigma) = \frac{e^{\left(\frac{\alpha - \mu}{2}\right)}}{\sigma \left(1 + e^{\left(\frac{\alpha - \mu}{2}\right)}\right)^2}; \; -\infty < \alpha < \infty. \quad (11)$$

The **Generalized extreme value (Gev) PDF**, which is defined as

$$f(\alpha \mid \nu, \mu, \sigma) = \left(\frac{1}{\sigma}\right) e^{-\left(1 + \nu \frac{(\alpha - \mu)}{\sigma}\right)^{-\frac{1}{\nu}}} \left(1 + \nu \frac{(\alpha - \mu)}{\sigma}\right)^{-1 - \frac{1}{\nu}}, \quad (12)$$

combines three distributions in one by case distinction: $\nu = 0$ corresponds to the type I case (Gumbel type), $\nu > 0$ to the type II case (Frechét type), and $\nu < 0$ to the type III case. Here, only the type III case, which corresponds to the reversed Weibull distribution, was present.

Periodic probability density functions

Inspired by Wahlström ([2009](#)), the following three periodic PDFs were examined for their goodness of fit. Here, they were defined for angles α ranging from 0 to π.

The **2-Cosine PDF** (Perkins and Mark [1981](#))

$$f(\alpha \mid \mu, \eta_1, \eta_2) = \frac{1}{\pi}\left(1 + \eta_1 \cos(2(\alpha - \mu)) + \eta_2 \cos(4(\alpha - \mu))\right) \quad (13)$$

considers the first and second term of the multi term cosine function suggested in (Cox [1952](#)). The parameter μ describes the location, and the two shape parameters, η_1 and η_2, must be chosen so that no negative function values arise. When only the first term is taken into account the function reduces to the 1-Cosine PDF (Corte and Kallmes [1962](#)). This was also tested, but it did not achieve the best results in any of the distributions considered here.

The **von Mises PDF** corresponds to the normal distribution for the periodic case. To describe the microstructural fiber orientation, it was slightly modified in (Perkins and Mark [1981](#)) to

$$f(\alpha \mid \mu, \kappa) = \frac{1}{\pi I_0(\kappa)} e^{\kappa \cos(2(\alpha - \mu))} \text{ with } \kappa > 0, \quad (14)$$

where the location of the function is prescribed by μ and where $I_0(\kappa)$ is the modified Bessel function of first type and order zero. The parameter κ is a measure of the concentration and correlates reciprocally to the variance σ^2 (measure of dispersion) in the normal distribution.

The **Elliptical PDF**

$$f(\alpha \mid \mu, C) = \frac{1}{\pi}\left(\frac{\sqrt{C}}{\cos^2(\alpha - \mu) + C \sin^2(\alpha - \mu)}\right) \text{ with } C > 0, \quad (15)$$

is presented here in the form Wahlström ([2009](#)) derived from stress/strain analysis. It is a representative of various fiber orientation distribution functions used in the literature (Prud'homme et al [1975](#); Schulgasser [1985](#); Wahlström [2009](#)), which can be converted into each other by adjusting the shape parameter C.

PDF selection approach

In order to find the probability density functions (PDFs) that best approximate the distribution of the in-plane orientation angles, as shown in Fig. [12](#), a two-step approach was followed.

First, the functional parameters of the non-periodic and periodic PDFs such as location or shape parameters were determined. This was done using a maximum likelihood estimation (MLE) method. For the non-periodic function type, a pool of 17 different functions (the above-mentioned and, among others, Normal distribution, Rician distribution or Rayleigh distribution) was present (de Castro [2023](#)). Based on the log-likelihood of each function calculated in MLE, the six non-periodic functions with the largest log-likelihoods were preselected. For the determination of the most suitable periodic function, a preselection was not necessary since only the four periodic functions mentioned above were examined.

In the second step, the goodness of fit of the functions, which were characterized by the previously

determined function parameters, was evaluated. The sum of squared errors (SSE) was used as a measure of the goodness of fit. To calculate this, the PDFs had to be transformed into cumulative density functions (CDFs). As exemplary shown in Fig. 14, using a standard normal distribution and 20 empirical data points, the distance ΔF between the empirical data $F_n(x)$ and the corresponding point of the approximated function $F_0(x)$ was determined. The normed sum of the squared distances of all data points n resulted in the SSE with

$$SSE = \frac{1}{n} \sum_{j=1}^{n} \left(|F_n(x_j) - F_0(x_j)| \right)^2. \qquad (16)$$

The non-periodic and periodic functions with the lowest SSEs were selected as the best fitting function of their type. This quantitative selection criterion coincided with the qualitative visual impression of the goodness of fit.

Choosing the goodness-of-fit criterion

The choice of the SSE method as a goodness-of-fit criterion was preceded by testing the suitability of other goodness-of-fit tests. In particular, the suitability of the Kolmogorov-Smirnov (KS) test was analyzed, because it quantitatively and absolutely states the goodness of the fit by calculating the p-value. The KS test postulates the null hypothesis that the empirical distribution originates from the tested distribution function. On the basis of a previously defined significance level α_s, this null hypothesis is to be rejected or not by comparing the p-value with the significance level. The p-value is based on the test statistic D_n with

Fig. 14 Cumulative densities of 20 data points represented as their discrete empirical values and approximated by a standard normal CDF. The distance between a data point and the functional approximation is highlighted by ΔF

$$D_n = \sup\left(|F_n(x) - F_0(x)| \right), \qquad (17)$$

for which the largest deviation of the empirical data $F_n(x)$ and the cumulative distribution function $F_0(x)$ is determined. If the p-value is less than α_s, the null hypothesis must be rejected with a probability of error of less than α_s. If the p-value is larger than α_s, the null hypothesis cannot be rejected. It is therefore assumed that the empirical data can be represented by the tested functional distribution. When applied to the available data of the in-plane orientation angle φ here, p-values far below 0.05 resulted for almost all 40 samples, although there was a good visual match between the empirical data and the tested functions. This effect was attributed to the large sample size of over 20,000 data points, since deviations between the distributions become more significant as the sample size increases. This effect can also be observed in other statistical goodness-of-fit tests in which the p-value is used to assess the goodness of fit. Therefore, this type of goodness-of-fit test was rejected, and the sum of squared errors method was utilized. It permits a quantitative but relative comparison between the analyzed functions. Nevertheless, compared to the KS test which evaluates just the largest error between two distributions, the SSE method includes each observation in the error calculation.

From orientation distribution function to orientation tensor

In the numerical microstructural modeling of fiber network structures, orientation distribution functions are often used to prescribe the orientation state of the fibers. Therefore, the focus in this work is on finding the best functional approximation of the fiber orientation in paperboard. However, in macrostructural constitutive modeling the concept of orientation or structural tensors is often used to incorporate material anisotropy into the model, such as in Li et al (2016) and Orgéas et al (2021). Figure 15 shows the relationship between the orientation distribution function, the fiber alignment in a microstructure and the corresponding orientation tensor. A very narrow distribution function (blue curve), which is close to a Dirac delta function, represents a fiber orientation state where the fibers are nearly parallel and where the corresponding orientation tensor has the shown form. It should be mentioned that a planar orientation state is assumed in the illustration, so
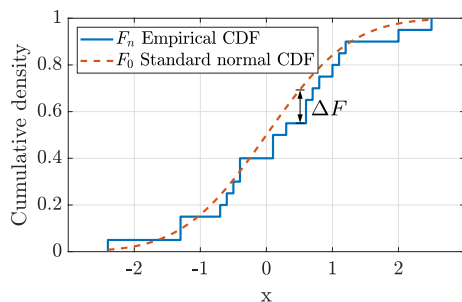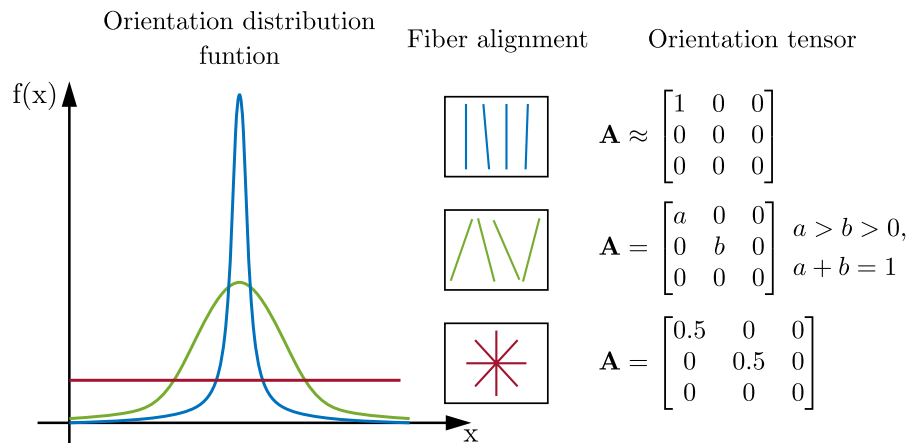
Fig. 15 Illustration of three fiber distributions as orientation distribution function, fiber alignment sketches and approximated orientation tensors

that the components of the third direction in the orientation tensor are zero. As the randomness of fiber orientation increases (green) up an isotropic orientation state (red), the orientation distribution functions become wider towards a constant line and the components of the orientation tensor change as shown.

Based on Equation (1), the second-order orientation tensor **A** can be calculated from the orientation distribution function. For a detailed description of the calculation steps, Gasser et al (2005) is recommended. There, a three-dimensional fiber orientation state is present. Since we assume planar fiber orientation, as elucidated in Sect. Orientation angles, the orientation tensor reduces from a three-by-three to a two-by-two tensor. With the fiber orientation unit vector $\mathbf{p} = \cos(\varphi)\,\mathbf{e}_1 + \sin(\varphi)\,\mathbf{e}_2$, the components of the orientation tensor **A** are calculated as

$$A_{11} = \int_0^\pi f(\varphi)\cos^2(\varphi)\,\mathrm{d}\varphi\,, \tag{18}$$

$$A_{22} = \int_0^\pi f(\varphi)\sin^2(\varphi)\,\mathrm{d}\varphi\,, \tag{19}$$

$$A_{12} = \int_0^\pi f(\varphi)\cos(\varphi)\sin(\varphi)\,\mathrm{d}\varphi = A_{21}\,. \tag{20}$$

Results

The fiber orientation analysis focused on two main aspects. On the one hand, it was investigated which PDFs are suitable for reproducing the in-plane fiber

distribution within an entire sample, without differentiation between the plies, but with special attention to the original position of the sample in the paper roll (edge, center). On the other hand, the fiber distribution within the three plies (top, middle, bottom) of each sheet was examined in order to investigate structural differences between the plies and their effect on the PDF choice.

Fiber orientation in sample

First, the distribution of the fiber orientation within the sample was considered without differentiating between the plies. The fiber orientation distribution, which was considered as the distribution of the in-plane angle φ_1 toward the first principal direction $\mathbf{v}_1$ of all evaluation cells, was approximated by probability density functions. In a previous study (Kloppenburg et al 2023a), the orientation distribution was approximated by non-periodic PDFs. In this paper, the application and investigation of periodic PDFs is added and the results are compared with the previous ones.

Based on the PDF selection procedure described above, the best non-periodic and periodic PDFs were determined and are shown in Figs. 16 and 17. The letters A to E indicate the five paper rolls, from each of which eight samples were taken; four from the edge and four from the center of the paper roll. The angular distributions of the in-plane angle φ_1 are shown as histograms and with their functional description. Considering the non-periodic PDFs (Fig. 16), the blue curves with an additional circle are t-location scale PDFs, the violet ones with a square are Logistic

Fig. 16 The orientation distributions of the in-plane angle φ_1 toward the first principal direction $\mathbf{v}_1$ are shown as histograms and non-periodic PDFs. With reference to Fig. 3, it is illustrated from which paper roll and from location in the paper roll the samples originate. The histograms are approximated by the t-location scale PDF (blue, circle), by the Logistic PDF (violet, square) or by the Generalized extreme value PDF (dark purple, triangle)
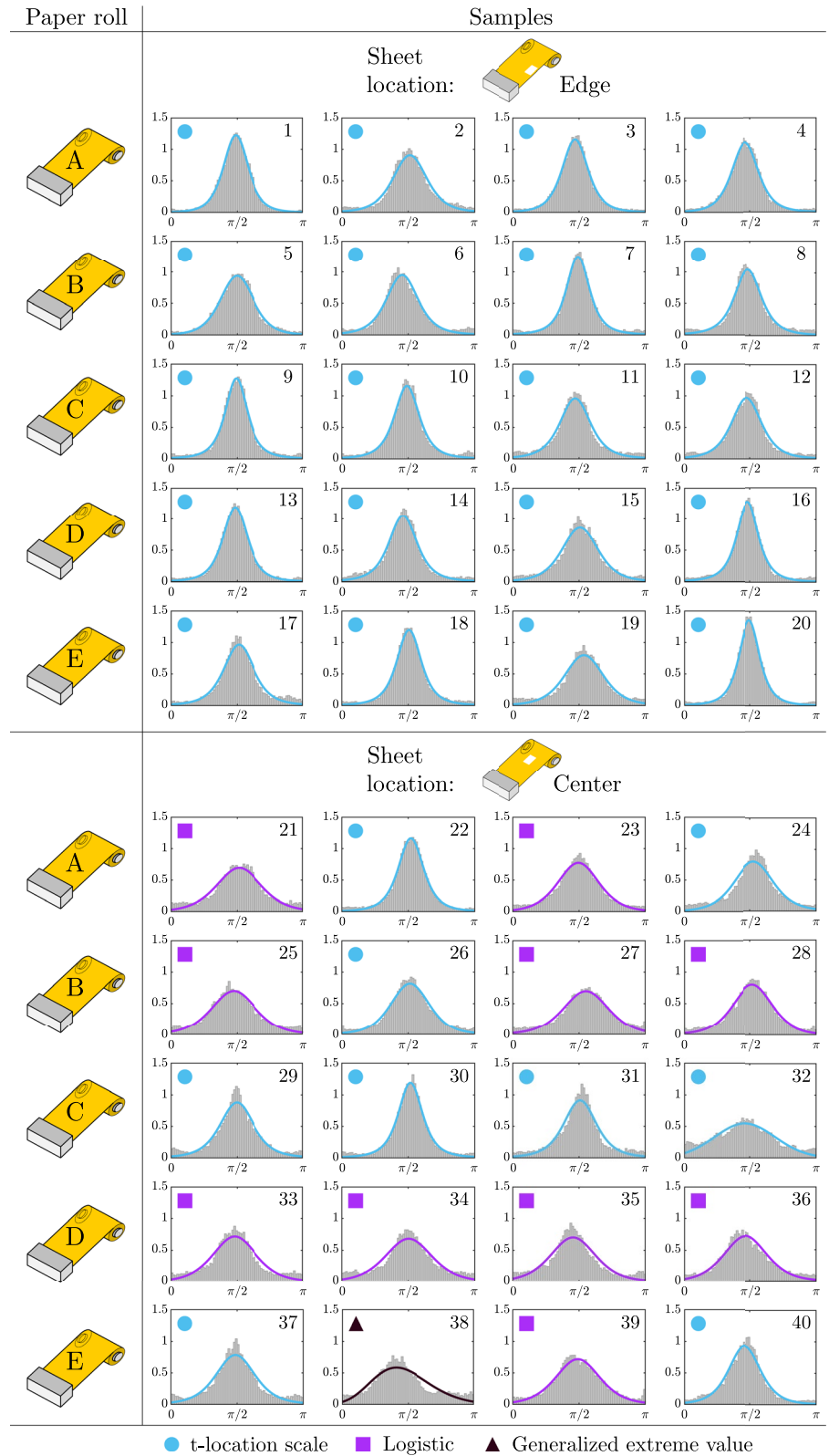
Fig. 17 The orientation distributions of the in-plane angle φ_1 toward the first principal direction $\mathbf{v}_1$ are shown as histograms and periodic PDFs. With reference to Fig. 3, it is illustrated from which paper roll and from location in the paper roll the samples originate. The histograms are approximated by the von Mises PDF (red, circle), by the Elliptical PDF (green, square) or by the 2-Cosine PDF (yellow, triangle)
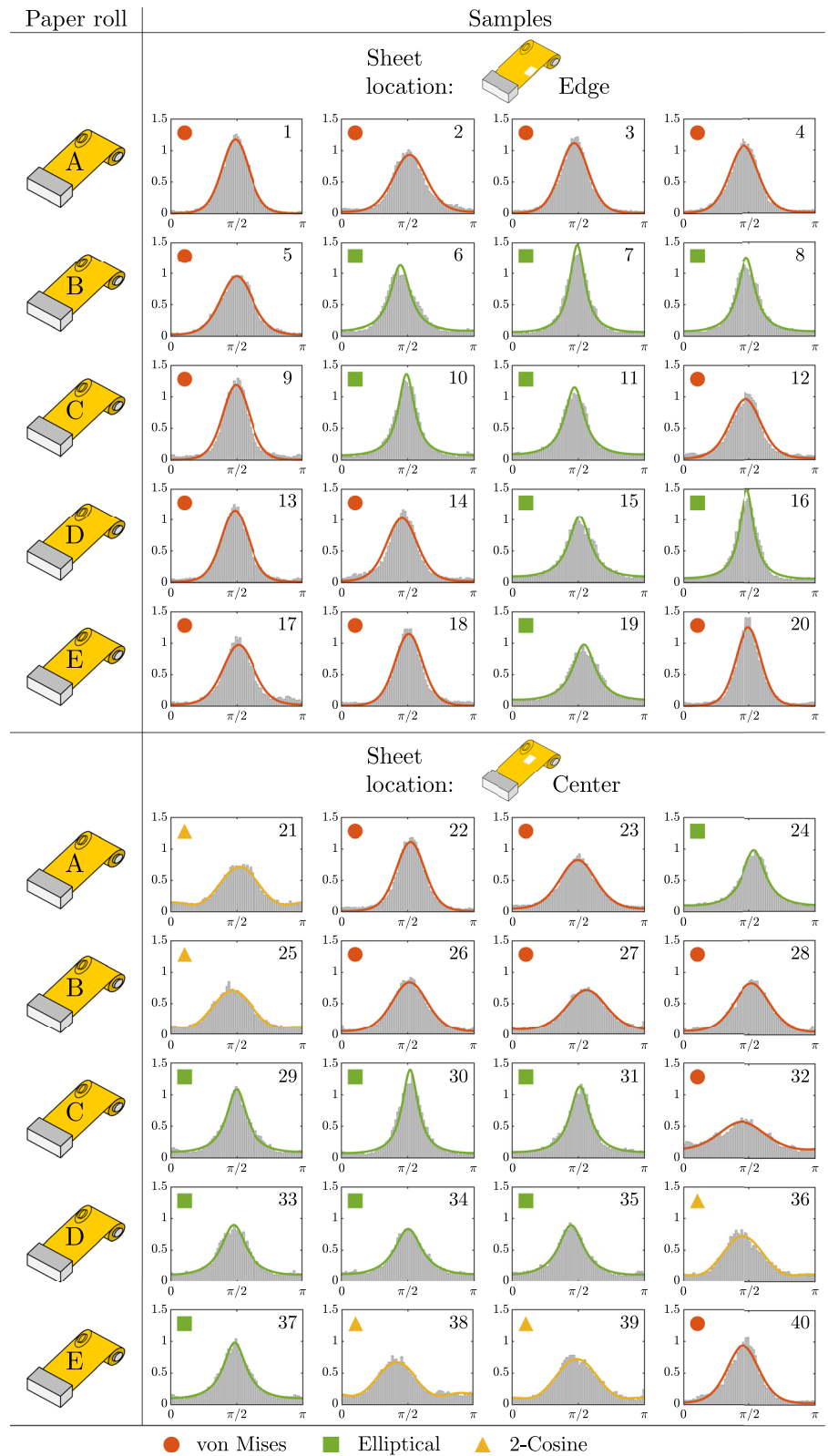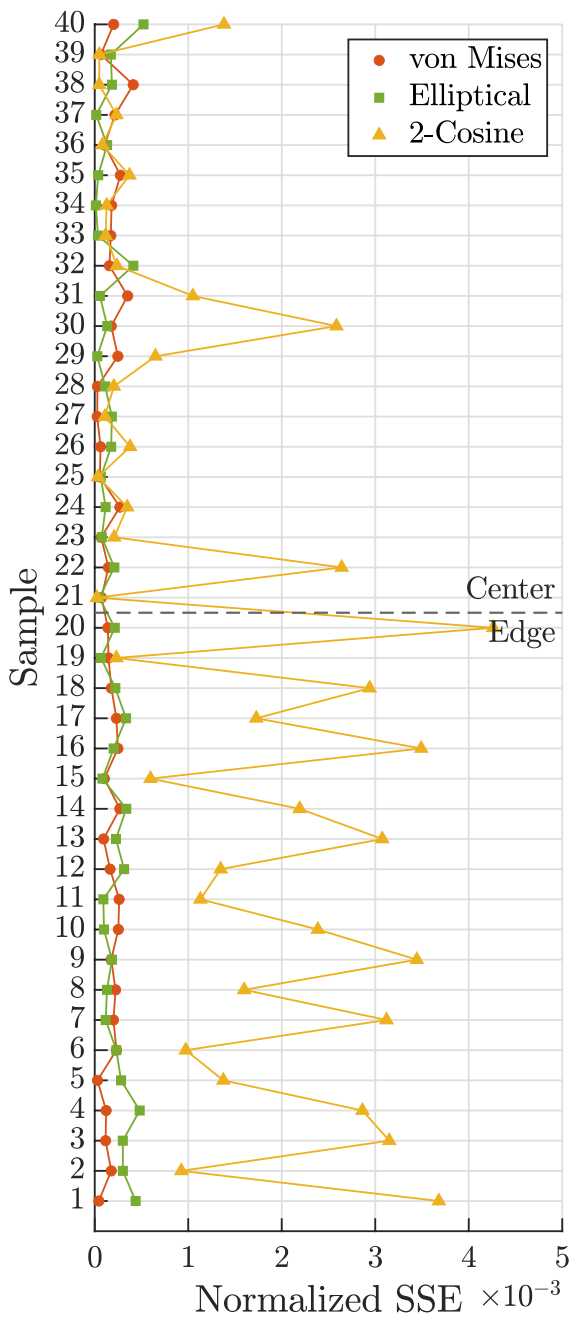
Fig. 18 Normalized SSEs of periodic PDFs

Fig. 19 Normalized SSEs of non-periodic PDFs

PDFs and the dark purple curve with a triangle is the Gev PDF. In Fig. 17, the results of testing periodic PDFs are presented. There, the red colored curves are von Mises PDFs, which are additionally marked with a red circle. The green curves marked with a square
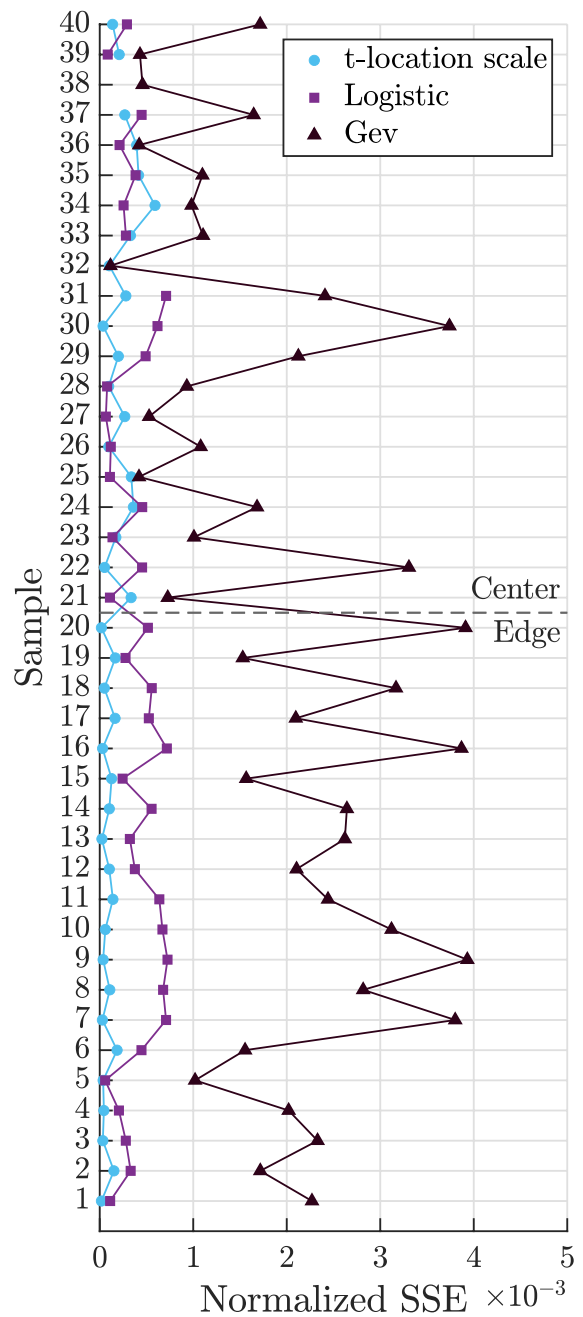
are Elliptical PDFs and the yellow ones with triangles are 2-Cosine PDFs.

The quality of the individual periodic and non-periodic PDFs evaluated on the basis of their normalized sum of squared errors (SSE) is shown in Figs. 18, 19 and 20. Samples 1 to 20 originated from the edge

and samples 21 to 40 from the center. In addition to the three PDF types shown in Fig. 18 and 19, other types were also examined, particularly in the case of the non-periodic PDFs. However, only the results of the PDFs that showed the smallest error for at least one sample and thus best represented the histograms of the angular distributions are shown here. For some samples, such as sample 38, it happened that one or two of the listed non-periodic PDF types were already eliminated in the preselection step. Therefore, their SSE is not displayed. To compare both PDF approaches, Fig. 20 compares the SSE of the best periodic and non-periodic PDF per sample. In addition, the mean SSE values of each PDF and of the both PDF approaches are plotted as vertical lines. Since the mean SSE value of the 2-Cosine and Gev PDFs was much greater than that of the others, the line is outside the range shown, but the mean SSE value is provided in the legend. The exact SSE values and function parameters for the best periodic and non-periodic PDFs are given in Appendices Tables 2 and 3.

Fiber orientation in plies

The second focus was on the analysis of the fiber orientation distribution in the paperboard plies. As described in Sect. Material, the tested paperboard consisted of three differently composed plies (top, middle, bottom). They differed not only in the fiber types, but also in the fiber volume fraction, as exemplified in Fig. 21. There, the fiber volume fraction of samples 1 to 4 is plotted against the sample thickness. It is noticeable that the top and bottom plies, which were about 100 µm thick, had a much higher density than the middle ply. This led to the question of whether the fiber orientation in the plies also differed.

For this analysis, only periodic probability density functions were tested. They were able to cover pronounced baselines better than the non-periodic PDFs, which will be elucidated in Sect. Discussion - Fiber orientation in sample.

In contrast to the analysis in Sect. Results - Fiber orientation in sample above, the four samples of a sheet are now merged into a data set in which the fiber orientation is examined separately for each ply. The sketch in Fig. 3 explains which samples are combined: Two sheets were taken from each paper roll A, B, C, D, and E, one from the edge and one from the center, resulting in a total of ten sheets. In turn, four samples were cut from each of the sheets.
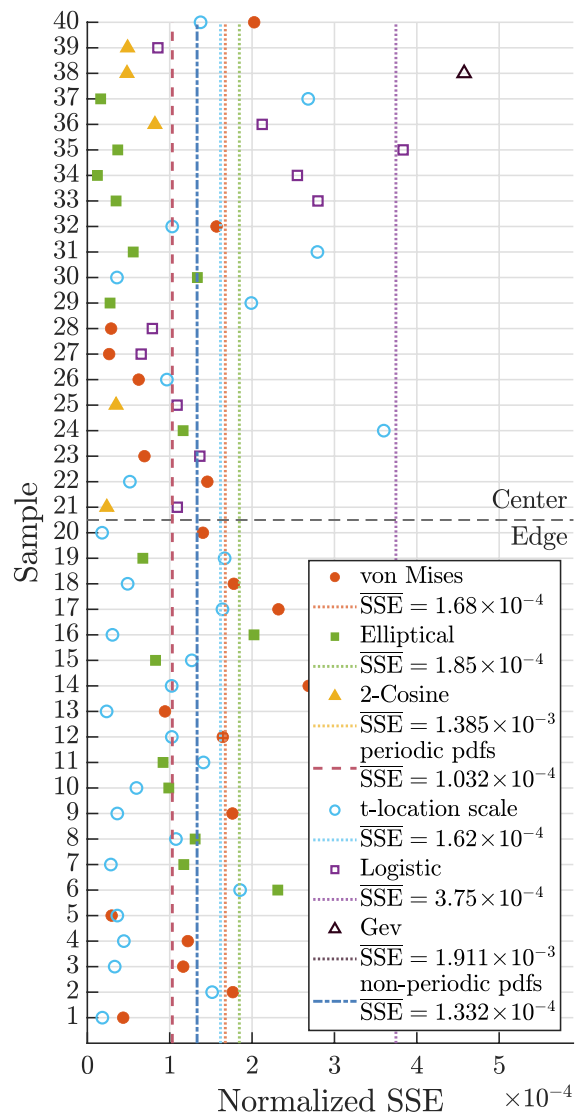

Fig. 20 Normalized SSEs of best periodic PDF in contrast to best non-periodic PDF

For the analysis of the fiber orientation in the plies, the in-plane orientation angles φ_1 of the four samples were merged into the "sheet data set". Then, the best periodic PDFs for the angular distribution in the individual plies per sheet were determined.

Table 1 lists the PDFs determined for the plies of all 10 sheets and gives the total normalized SSE per ply. In Appendix Table 4, also the PDF's function parameters and each SSE are given. In most cases, the von Mises and Elliptical PDFs approximated the fiber orientation distribution best.
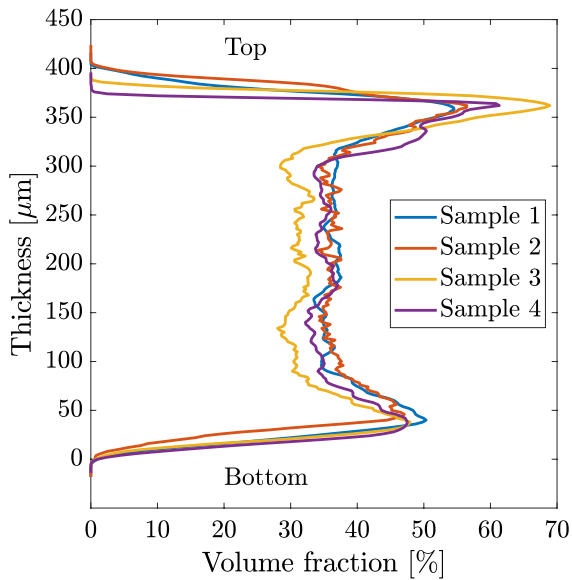
Fig. 21 Fiber volume fraction against sample thickness of samples 1 to 4

Table 1 Number of each periodic probability density function (PDF) best approximating the fiber orientation distribution in the three paperboard plies. The angular data of the four samples per sheet are merged into a sheet data set resulting in a total of ten data sets. Added is the normalized sum of squared errors (SSE) per ply, summed over all data sets

PDF	Top ply	Middle ply	Bottom ply
von Mises	2	10	2
Elliptical	7	0	8
2-Cosine	1	0	0
SSE per ply	$2.01 \cdot 10^{-3}$	$1.06 \cdot 10^{-3}$	$1.26 \cdot 10^{-3}$

However, it was noticeable that the von Mises PDF works better for the middle ply and the Elliptical PDF for the outer plies. This tendency can be seen in Fig. 22 where the fiber orientation distribution per ply is shown as histograms and PDFs.

Discussion

Section Results presented the best PDFs based on their sum of squared errors (SSE). The following section addresses the choice of the PDF type (periodic, non-periodic) to describe the fiber orientation, differences in the fiber orientation between samples from

Fig. 22 From each paper roll A to E, two sheets (edge and center) were taken and the fiber directions in each ply were analyzed. The illustrations of paper rolls, sheet location and paperboard plies follow Figs. 3 and 4. In the table, the orientation distributions of the in-plane angle φ_1 toward the first principal direction $\mathbf{v}_1$ are shown as histograms and periodic PDFs. The histograms were approximated by the von Mises PDF (red, circle), by the Elliptical PDF (green, square) or by the 2-Cosine PDF (yellow, triangle)

the edge and from the center of a paper roll as well as differences between the paperboard plies.

Fiber orientation in sample

The comparison of the SSE results of the PDF approaches in Fig. 20 shows that half of the samples are better approximated with periodic PDFs and the other half with non-periodic PDFs. In particular, the angular distributions at the edge of the paper roll, which are often ideally bell-shaped with almost no baseline, are mostly best represented by the t-location scale PDF (non-periodic). This PDF type is characterized by three function parameters and is therefore more adaptable than the tested periodic functions with two function parameters. However, periodic functions perform significantly better for distributions with a pronounced baseline, as they occur in the center of the paper roll and also in outer plies of the paperboard (Fig. 22). Furthermore, considering the mean SSE of both PDF types across all 40 samples, as highlighted in Fig. 20, periodic PDFs are overall better suited to approximate the fiber orientation distribution than non-periodic PDFs. Hence, the evaluations in this and the following section will focus on the periodic PDFs.

Choice of best periodic PDF for entire samples

The von Mises and the Elliptical PDF were able to represent the orientation distribution similarly well, as can be seen from the low SSEs in Fig. 18. Clearly, the von Mises PDF was the best choice for nearly normally distributed orientation angles. Moreover, this PDF worked well for distributions with a more pronounced baseline and wide waist combined with a smooth transition from bell shape to baseline (e.g. sample 27 in Fig. 17). The Elliptical PDF, however, worked best for distributions with a narrow waist. Only some distributions of samples from the center
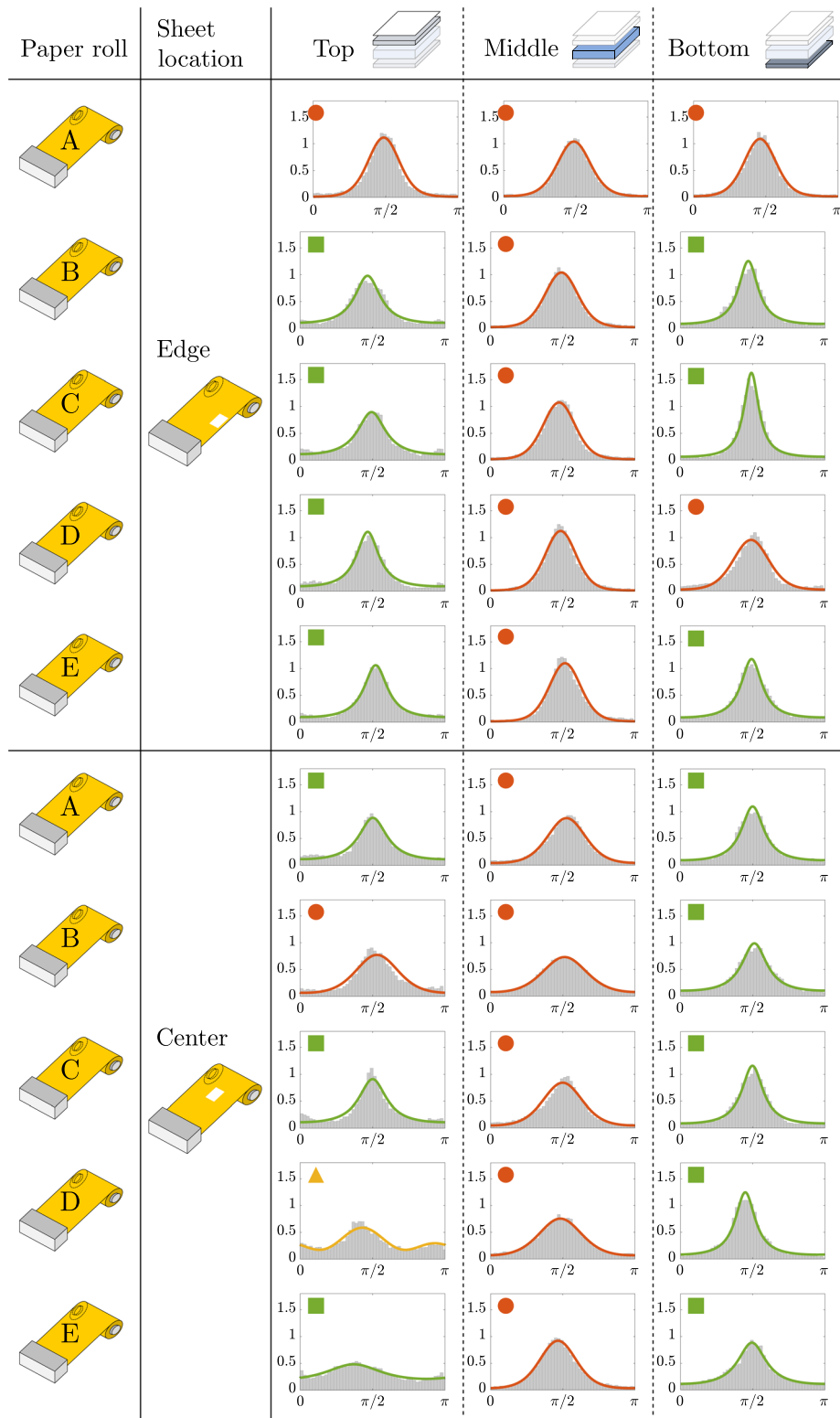
could better be realized with the 2-Cosine PDF. Noticeable from the curves in Fig. 17, these distributions had a pronounced and partly irregular baseline and a wide waist. In general, all periodic PDFs were able to display distributions with distinct baselines, which was not possible to the same extent for non-periodic PDFs.

Fiber orientation variation in a paper roll

The analysis focus is now shifted to the variation of the fiber orientation within a paper roll. Looking at the histograms in Fig. 17, it is already noticeable that, compared to the samples from the edge of the paper roll, the samples from the center have a more pronounced baseline, which indicates a higher in-plane isotropy. In order to examine such characteristics quantitatively, the function parameters are analyzed. For this purpose, all distributions are approximated by the von Mises PDF. Although this was not always the best choice (see Fig. 17), it still allows a comparison between the features of the φ_1-distribution of the samples, such as the location of the peak and the width of the waist. Figure 23 shows an example of the case where the von Mises PDF was used instead of the more appropriate Elliptical PDF and it can be seen that the histogram characteristics, such as peak location, are still approximately matched.

The von Mises PDF consists of two function parameters: (i) location parameter μ, which specifies the position of the distribution peak, indicating the main fiber orientation, (ii) concentration parameter κ, which defines the width of the distribution, indicating the degree of fiber orientation randomness. To visualize the distribution of the functional parameters, boxplots were used in Figs. 24 and 25.

The distributions of the location parameter μ in Fig. 24 show that the preferred fiber direction is similar in both paper roll locations. However, in both parts of the paper roll, the pronounced fiber direction is not exactly in machine direction at 90° or $\frac{\pi}{2} \approx 1.571$. Instead, the mean and median value of the location parameters in the edge samples are 1.533 and 1.534, which corresponds to 87.83° and 87.89°. In the center
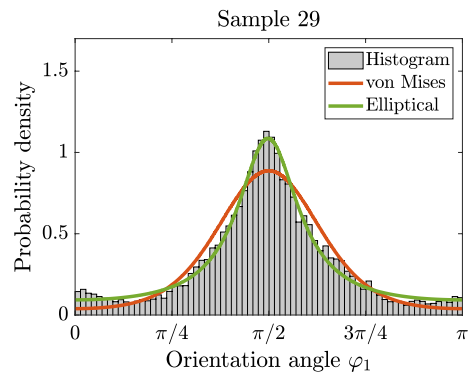

Fig. 23 Example for approximating the fiber orientation distribution with the von Mises PDF instead of the more appropriate Elliptical PDF
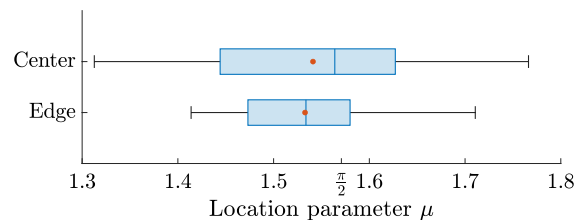

Fig. 24 Distribution of the location parameter μ of the von Mises PDF approximating the fiber distributions in samples from the center and the edge of the paper roll
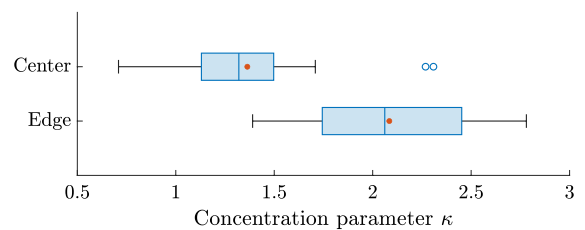

Fig. 25 Distribution of the concentration parameter κ of the von Mises PDF approximating the fiber distributions in samples from the center and the edge of the paper roll

of the paper roll, the deviation from the machine direction is smaller. Here, the mean value is 1.541

(88.29°) and the median is 1.564 (89.61°). The scatter of the location parameter, expressed by the box edges showing the 25th and 75th percentiles, is much smaller at the edge than in the center. Even the most extreme values, represented by the whiskers, are closer together at the edge of the paper roll than in the center. This means that the variation of the preferred fiber direction is greater in the paper roll center than at the edge.

Furthermore, the concentration parameter κ is analyzed and its distribution is shown in Fig. 25. The concentration parameters determined for the edge samples are larger than those for the samples from the center. This means that the distributions in samples from the edge are narrower and that the fiber anisotropy is more pronounced there. In the center, however, a more random fiber orientation can be observed. There are only two outliers, shown as blue circles, which lie in the same area as the box of the edge data. The remaining concentration parameters are smaller than most of the parameters in the edge samples. This illustrates the large difference in the degree of anisotropy of the fiber orientation at the edge and in the center of the paper roll.

Fiber orientation in plies

The following elucidates why the periodic PDF types, describing the fiber orientation distributions, differ in the three paperboard plies. Moreover, as before, the von Mises distribution was used to approximate all fiber distributions in order to take a closer look at their function parameters. This allows drawing conclusions about the regularity of the distribution shapes and the degree of anisotropy in the plies.

Choice of best periodic PDF for paperboard plies

The table in Fig. 22 shows the histograms of the in-plane orientation angle φ_1 for each ply of each sheet and the respective best periodic PDFs. In the bottom ply, the histograms have a bell shape, but also a constant baseline. Since most of the distributions change abruptly between bell shape and baseline and also have a narrow waist and a sharp distribution peak, the Elliptical PDF is best suited for the bottom ply. Eight of the ten bottom

ply distributions are best approximated by the Elliptical PDF. For two distributions with a wider waist and a less pronounced baseline the von Mises PDF was more appropriate.

Such distributions (wider waist, less pronounced baseline) are mainly found in the middle plies, where the von Mises PDF was the best choice in all cases. Here, it is noticeable that the baseline is much lower than in the outer plies and that the distributions have a smoother transition between bell shape and baseline.

The most pronounced baseline could be found in the top ply. A coating was applied to the outside of this ply in a final manufacturing step. Here, it was not possible to distinguish between fibers and coating particles during image postprocessing so that particles might have been erroneously declared as fibers. Since the particles are not oriented, the baseline of the φ_1-distribution, which represents the fiber orientation isotropy, is enlarged. As with the bottom ply, most distributions were best approximated by the Elliptical PDF (seven out of ten). Only when the distribution is asymmetric and has an irregular baseline (sheet: D-center), the 2-Cosine PDF works better, or when the distribution is slightly broader, the von Mises PDF is a better choice (sheet: A-edge, B-center). It is particularly noticeable that some distributions in the top ply are even approximately isotropic (sheet: D-center, E-center). Based on the normalized SSE per ply summed over all 10 paper roll sheets in Table 1, the most accurate functional approximation was obtained for the middle ply and the least accurate for the top ply.

Fiber orientation variation in paperboard plies

Subsequently, all 30 ply-wise sheet data sets (ten per ply) were approximated by the von Mises PDF to analyze the distribution of their function parameters, as described in Sect. Discussion - Fiber orientation in sample. Figure 26 shows the results in the form of boxplots. It should be mentioned that a data set of 10 evaluated von Mises PDFs per ply is relatively small for a statistical analysis. Nevertheless, some peculiarities in the fiber orientation distribution can still be derived from the investigation of the location and concentration parameters.

The location parameter of the von Mises PDF represents the location of the distribution peak. It is noticeable
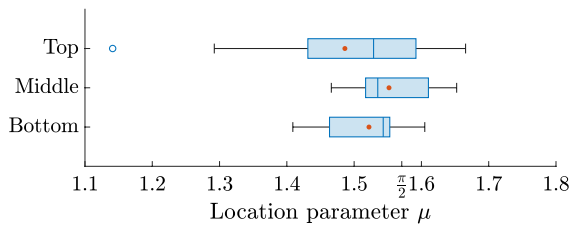
Fig. 26 Distribution of the location parameter μ of the von Mises PDF approximating the fiber distributions in the top, middle and bottom ply of the 10 sheets (combination of four samples per sheet) from the paper roll A to E

Fig. 27 Distribution of the concentration parameter κ of the von Mises PDF approximating the fiber distributions in the top, middle and bottom ply of the 10 sheets (combination of four samples per sheet) from the paper roll A to E
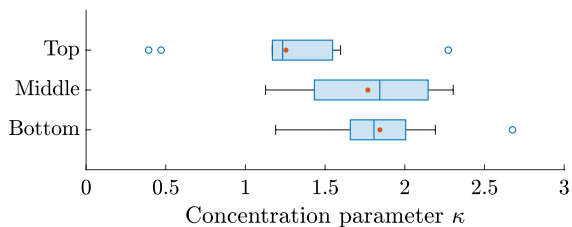
that the median with a value of around 1.53, which corresponds to 87.7°, is similar in all plies. If the analyzed data set is small, the mean value can be more strongly influenced by outliers. Therefore, the median as the value in the middle of the data set is the better parameter for interpretation and thus chosen here. In the bottom and middle ply, the variation of the location parameter represented by the box size and whisker length is much smaller than in the top ply. This means that the preferred direction in the bottom and middle ply is more stable across the sheets.

How wide the distribution of the in-plane angle φ_1 is and thus how pronounced the anisotropy of the fiber orientation is, can be derived from the concentration parameter κ of the von Mises PDF shown in Fig. 27. The largest concentration parameters are found in the bottom and middle ply with a median of 1.81 and 1.84. This means that the distributions have a narrow waist and thus a pronounced fiber orientation towards the preferred direction.
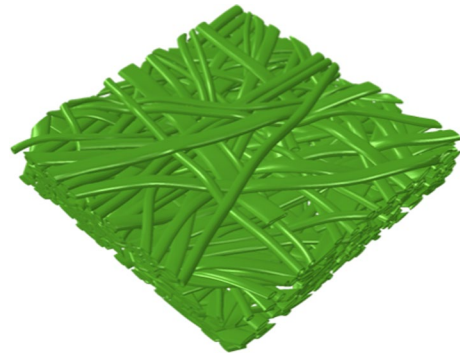

Fig. 28 Numerical model of a paper microstructure

The variation of this parameter is lowest in the bottom ply which is displayed by the box size and whisker length. This means that the fiber distribution in the bottom ply was quite similar for all sheets. In the top ply, the median of the concentration parameter is 1.23 and the box and whiskers overlap only slightly with those of the bottom and middle ply. This indicates a more random fiber orientation in the top than in the bottom and middle ply. However, this could be explained by the influence of the coating as mentioned before.

Conclusion and outlook

Based on high-resolution µ-CT scans, a concept was developed to calculate the fiber orientation distribution using orientation tensors and to translate these distributions into non-periodic and periodic probability density functions (PDFs). On the one hand, PDFs for the fiber orientation state in a sample, without differentiation between plies, were found depending on its original position in the paper roll. On the other hand, PDFs were determined for each individual paperboard ply.

If non-periodic PDFs are used to approximate the fiber orientation distribution, the t-location scale PDF was the most suitable one. It showed the highest adaptability based on the three function parameters. Considering periodic PDFs, it was shown that the von Mises PDF is best suited for nearly normally

distributed fiber orientation distributions and that the Elliptical PDF should be used if the distribution has a narrower waist or a more pronounced baseline. Non-symmetric distributions are best approximated by the 2-Cosine PDF. These selection criteria can also be applied to the fiber orientation distributions in the individual plies. It turned out that the Elliptical PDF should be taken for the outer plies and the von Mises PDF for the middle ply.

In this paper, the equations for the discussed non-periodic and periodic PDFs as well as the corresponding functional parameters determined for the investigated samples are given. Thus, they can be easily used in numerical fiber network models as shown in Fig. 28 to represent the paperboard microstructure as accurately as possible.

Two details should be mentioned that may have an influence on the results shown. In contrast to other studies found in the literature about fiber orientation in paper, the angular distributions shown do not represent the angles of detected individual fibers, but of the first principal directions of the orientation tensors, which smear the orientation state in an evaluation cell. The extent of this difference should be investigated in a future study. To do so, the same PDF determination method should be applied to CT scans where the direction of individual fibers is measured. Another detail is that the coating on the top side of the examined paperboard could lead to an overestimation of the fiber orientation randomness in this ply. However, coating is used in most practical applications and should therefore also be integrated into the consideration.

From a numerical mechanics point of view, the effect of using different PDFs to represent the same microstructure within a fiber network simulation should be quantified and the effect of using different PDFs in each paperboard plies should be investigated.

Data availability The data and codes used in the presented manuscript are available upon reasonable request from the corresponding author.

Declarations

Conflict of interest The authors have no relevant financial or non-financial interests to disclose.

Appendix A

See Tables 2, 3, 4

Table 2 Periodic probability density functions (PDF) that best approximate the distribution of in-plane angles φ_1 toward the orientation tensor's first principal direction $\mathbf{v}_1$. For each sample the best PDF, the normalized sum of squared errors (SSE) and the first, second and third function parameter is given.

The meanings of the function parameters are described in Sect. Orientation distribution functions and are briefly stated here in ascending order: von Mises PDF: location (μ), concentration (κ), Elliptical PDF: location (μ), shape (C), 1- and 2-Cosine PDF: location (μ), shape (η_1, η_2)

Sample	Periodic PDF	SSE [$\cdot 10^{-4}$]	Parameter 1	Parameter 2	Parameter 3
1	von Mises	0.435	1.536	2.492	
2	von Mises	1.766	1.614	1.694	
3	von Mises	1.164	1.471	2.287	
4	von Mises	1.219	1.439	2.128	
5	von Mises	0.295	1.566	1.756	
6	Elliptical	2.312	1.396	12.577	
7	Elliptical	1.171	1.546	21.216	
8	Elliptical	1.309	1.505	15.341	
9	von Mises	1.762	1.552	2.545	
10	Elliptical	0.989	1.540	18.317	
11	Elliptical	0.919	1.479	13.139	
12	von Mises	1.644	1.475	1.796	
13	von Mises	0.943	1.527	2.413	
14	von Mises	2.687	1.433	1.980	
15	Elliptical	0.828	1.600	11.014	
16	Elliptical	2.023	1.513	21.805	
17	von Mises	2.320	1.614	1.820	
18	von Mises	1.778	1.594	2.390	
19	Elliptical	0.674	1.705	9.458	
20	von Mises	1.403	1.550	2.781	
21	2-Cosine	0.236	1.635	0.894	0.362
22	von Mises	1.457	1.635	2.269	
23	von Mises	0.693	1.557	1.381	
24	Elliptical	1.163	1.688	9.787	
25	2-Cosine	0.349	1.466	0.913	0.308
26	von Mises	0.623	1.615	1.428	
27	von Mises	0.265	1.766	1.091	
28	von Mises	0.289	1.629	1.372	
29	Elliptical	0.276	1.565	11.655	
30	Elliptical	1.336	1.627	19.127	
31	Elliptical	0.557	1.607	12.622	
32	von Mises	1.568	1.397	0.709	
33	Elliptical	0.349	1.495	7.954	
34	Elliptical	0.122	1.582	6.879	
35	Elliptical	0.369	1.399	7.884	
36	2-Cosine	0.820	1.417	0.961	0.323
37	Elliptical	0.162	1.521	9.502	
38	2-Cosine	0.481	1.300	0.757	0.347
39	2-Cosine	0.488	1.529	0.954	0.309
40	von Mises	2.026	1.424	1.709	

Table 3 Non-periodic probability density functions (PDF) that best approximate the distribution of in-plane angles φ_1 toward the orientation tensor's first principal direction $\mathbf{v}_1$. For each sample the best PDF, the normalized sum of squared errors (SSE) and the first, second and third function parameter is given. The meanings of the function parameters are described in Sect. Orientation distribution functions and are briefly stated here in ascending order: t-Location Scale PDF: location (μ), scale (σ), shape (ν), Logistic PDF: location (μ), scale (σ), Generalized extreme value (Gev) PDF: location (μ), scale (σ), shape (nu)

Sample	Non-periodic PDF	SSE [$\cdot 10^{-4}$]	Parameter 1	Parameter 2	Parameter 3
1	t-Location Scale	0.182	1.538	0.306	4.060
2	t-Location Scale	1.515	1.610	0.415	4.223
3	t-Location Scale	0.332	1.476	0.321	3.507
4	t-Location Scale	0.443	1.447	0.338	3.846
5	t-Location Scale	0.364	1.568	0.408	5.799
6	t-Location Scale	1.855	1.428	0.393	3.575
7	t-Location Scale	0.286	1.545	0.290	2.578
8	t-Location Scale	1.076	1.517	0.347	2.852
9	t-Location Scale	0.364	1.551	0.285	2.548
10	t-Location Scale	0.596	1.538	0.316	2.721
11	t-Location Scale	1.410	1.479	0.384	3.127
12	t-Location Scale	1.026	1.483	0.383	3.607
13	t-Location Scale	0.234	1.526	0.310	3.238
14	t-Location Scale	1.024	1.446	0.351	3.105
15	t-Location Scale	1.268	1.595	0.441	4.762
16	t-Location Scale	0.305	1.509	0.284	2.550
17	t-Location Scale	1.640	1.614	0.385	3.472
18	t-Location Scale	0.489	1.589	0.305	2.848
19	t-Location Scale	1.667	1.688	0.475	4.971
20	t-Location Scale	0.179	1.549	0.269	2.758
21	Logistic	1.092	1.618	0.360	
22	t-Location Scale	0.516	1.633	0.316	3.022
23	Logistic	1.366	1.555	0.323	
24	t-Location Scale	3.599	1.651	0.484	5.348
25	Logistic	1.090	1.491	0.356	
26	t-Location Scale	0.966	1.612	0.469	5.987
27	Logistic	0.654	1.733	0.358	
28	Logistic	0.789	1.622	0.316	
29	t-Location Scale	1.991	1.565	0.425	3.761
30	t-Location Scale	0.360	1.622	0.307	2.708
31	t-Location Scale	2.793	1.594	0.407	3.415
32	t-Location Scale	1.030	1.442	0.727	200
33	Logistic	2.800	1.512	0.347	
34	Logistic	2.550	1.579	0.366	
35	Logistic	3.834	1.428	0.355	
36	Logistic	2.123	1.449	0.345	
37	t-Location Scale	2.681	1.531	0.481	4.556
38	Gev	4.575	1.175	0.637	-0.162
39	Logistic	0.856	1.540	0.348	
40	t-Location Scale	1.375	1.435	0.403	4.253

Table 4 Periodic probability density functions (PDF) that best approximate the distribution of in-plane angles φ_1 toward the orientation tensor's first principal direction $\mathbf{v}_1$. The orientation angles φ_1 of the four samples taken from the edge or the center of paper roll A to E are combined to one dataset representing the sheet's fiber orientation. For each ply (top, middle, bottom) of a sheet the best PDF, the normalized sum of squared errors (SSE) and the first, second and third function parameter is given. The meanings of the function parameters (Param) are described in Sect. Orientation distribution functions and are briefly stated here in ascending order: von Mises PDF: location (μ), concentration (κ), Elliptical PDF: location (μ), shape (C), 2-Cosine PDF: location (μ), shape (η_1, η_2)

Paper roll	Comb. of samples	Ply	PDF	SSE [$\cdot 10^{-4}$]	Param 1	Param 2	Param 3
A: edge	1-4	Top	von Mises	1.926	1.529	2.273	
		Middle	von Mises	0.501	1.529	2.028	
		Bottom	von Mises	1.262	1.446	2.192	
B: edge	5-8	Top	Elliptical	0.921	1.462	9.472	
		Middle	von Mises	0.655	1.542	2.028	
		Bottom	Elliptical	1.447	1.474	15.577	
C: edge	9-12	Top	Elliptical	1.731	1.549	7.946	
		Middle	von Mises	1.137	1.491	2.147	
		Bottom	Elliptical	1.582	1.542	26.096	
D: edge	13-16	Top	Elliptical	4.113	1.465	12.086	
		Middle	von Mises	1.326	1.524	2.304	
		Bottom	von Mises	3.167	1.534	1.764	
E: edge	17-20	Top	Elliptical	0.224	1.639	11.131	
		Middle	von Mises	1.896	1.619	2.226	
		Bottom	Elliptical	0.908	1.545	13.683	
A: center	21-24	Top	Elliptical	1.580	1.578	7.725	
		Middle	von Mises	1.275	1.652	1.539	
		Bottom	Elliptical	0.720	1.568	11.894	
B: center	25-28	Top	von Mises	3.031	1.666	1.237	
		Middle	von Mises	0.090	1.610	1.126	
		Bottom	Elliptical	0.541	1.606	9.626	
C: center	29-32	Top	Elliptical	2.350	1.572	8.172	
		Middle	von Mises	2.202	1.568	1.433	
		Bottom	Elliptical	1.713	1.565	13.262	
D: center	33-36	Top	2-Cosine	3.677	1.350	0.454	0.387
		Middle	von Mises	0.409	1.517	1.193	
		Bottom	Elliptical	0.643	1.408	15.358	
E: center	37-40	Top	Elliptical	0.556	1.164	2.287	
		Middle	von Mises	1.064	1.466	1.658	
		Bottom	Elliptical	0.585	1.553	7.725	

References

Advani SG, Tucker CL (1987) The use of tensors to describe and predict fiber orientation in short fiber composites. J Rheol 31(8):751–784. https://doi.org/10.1122/1.549945

Alzweighi M, Mansour R, Lahti J et al (2021) The influence of structural variations on the constitutive response and strain variations in thin fibrous materials. Acta Mater 203(116):460. https://doi.org/10.1016/j.actamat.2020.11.003

Axelsson M (2008) Estimating 3d fibre orientation in volume images. In: 19th international conference on pattern recognition, pp 1–4

Bauer JK, Böhlke T (2021) Variety of fiber orientation tensors. Math Mech Solids 27(7):1185–1211. https://doi.org/10.1177/10812865211057602

Bauer JK, Schneider M, Böhlke T (2023) On the phase space of fourth-order fiber-orientation

tensors. J Elast 153(2):161–184. https://doi.org/10.1007/s10659-022-09977-2

Benítez AJ, Walther A (2017) Cellulose nanofibril nanopapers and bioinspired nanocomposites: a review to understand the mechanical property space. J Mater Chem A 5(31):16003–16024. https://doi.org/10.1039/c7ta02006f

Bosco E, Bastawrous MV, Peerlings RH et al (2015) Bridging network properties to the effective hygro-expansivity of paper: experiments and modelling. Philos Mag 95(28–30):3385–3401. https://doi.org/10.1080/14786435.2015.1033487

Bosco E, Peerlings R, Geers M (2015) Explaining irreversible hygroscopic strains in paper: a multi-scale modelling study on the role of fibre activation and micro-compressions. Mech Mater 91:76–94. https://doi.org/10.1016/j.mechmat.2015.07.009

Brandberg A, Motamedian HR, Kulachenko A et al (2020) The role of the fiber and the bond in the hygroexpansion and curl of thin freely dried paper sheets. Int J Solids Struct 193–194:302–313. https://doi.org/10.1016/j.ijsolstr.2020.02.033

Breuer K, Stommel M, Korte W (2019) Analysis and evaluation of fiber orientation reconstruction methods. J Compos Sci 3(3):67. https://doi.org/10.3390/jcs3030067

Bronkhorst C (2003) Modelling paper as a two-dimensional elastic-plastic stochastic network. Int J Solids Struct 40(20):5441–5454. https://doi.org/10.1016/S0020-7683(03)00281-6

Ceccato C, Brandberg A, Kulachenko A et al (2021) Micromechanical modeling of the paper compaction process. Acta Mech 232(9):3701–3722. https://doi.org/10.1007/s00707-021-03029-x

Charfeddine MA, Bloch JF, Mangin P (2019) Mercury porosimetry and X-ray microtomography for 3-dimensional characterization of multilayered paper: nanofibrillated cellulose, thermomechanical pulp, and a layered structure involving both. BioResources 14(2):2642–2650. https://doi.org/10.15376/biores.14.2.2642-2650

Chung DH, Kwon TH (2002) Invariant-based optimal fitting closure approximation for the numerical prediction of flow-induced fiber orientation. J Rheol 46(1):169–194. https://doi.org/10.1122/1.1423312

Cintra JS, Tucker CL (1995) Orthotropic closure approximations for flow-induced fiber orientation. J Rheol 39(6):1095–1122. https://doi.org/10.1122/1.550630

Corte H, Kallmes O (1962) Statistical geometry of a fibrous network, vol 1, Technical section of the british paper and board makers' association, pp 13–46

Cowin SC (1985) The relationship between the elasticity tensor and the fabric tensor. Mech Mater 4(2):137–147. https://doi.org/10.1016/0167-6636(85)90012-2

Cox HL (1952) The elasticity and strength of paper and other fibrous materials. Br J Appl Phys 3(3):72–79. https://doi.org/10.1088/0508-3443/3/3/302

de Castro F (2023) fitmethis. MATLAB central file exchange, https://www.mathworks.com/matlabcentral/fileexchange/40167-fitmethis

de Oliveira Mendes A, Fiadeiro PT, Ramos AMM et al (2013) Development of an optical system for analysis of the ink-paper interaction. Machine Vision Appl 24(8):1733–1750. https://doi.org/10.1007/s00138-013-0496-y

Decker J, Khaja A, Hoang M, et al (2013) Variation of paper curl due to fiber orientation. In: Application of imaging techniques to mechanics of materials and structures, Volume 4: Proceedings of the 2010 annual conference on experimental and applied mechanics, Springer, pp 347–352

Dias PA, Rodrigues RJ, Reis MS (2023) Fast characterization of in-plane fiber orientation at the surface of paper sheets through image analysis. Chemom Intell Lab Syst 234(104):761. https://doi.org/10.1016/j.chemolab.2023.104761

Enomae T, Han YH, Isogai A (2006) Nondestructive determination of fiber orientation distribution of paper surface by image analysis. Nordic Pulp Paper Res J 21(2):253–259. https://doi.org/10.3183/npprj-2006-21-02-p253-259

Fellers C, Carlsson L, Mark R et al (2001) Bending stiffness, with special reference to paperboard. Handbook Phys Test Paper 1:233–256

Fiadeiro P, Pereira M, Jesus M et al (2002) The surface measurement of fibre orientation anisotropy and misalignment angle by laser diffraction. J Pulp Paper Sci 28(10):341–346

Gasser TC, Ogden RW, Holzapfel GA (2005) Hyperelastic modelling of arterial layers with distributed collagen fibre orientations. J Royal Soc Interface 3(6):15–35. https://doi.org/10.1098/rsif.2005.0073

Görthofer J, Schneider M, Ospald F et al (2020) Computational homogenization of sheet molding compound composites based on high fidelity representative volume elements. Comput Mater Sci 174(109):456. https://doi.org/10.1016/j.commatsci.2019.109456

Görtz M, Kettil G, Målqvist A et al (2022) Network model for predicting structural properties of paper. Nordic Pulp Paper Res J 37(4):712–724. https://doi.org/10.1515/npprj-2021-0079

Hess T, Brodeur PH (1996) Effects of wet straining and drying on fibre orientation and elastic stiffness orientation. J Pulp Paper sci 22(5):J160-1164

Hirn U, Bauer W (2007) Evaluating an improved method to determine layered fibre orientation by sheet splitting. In: 61st Appita Annual conference and exhibition, Gold Coast, Australia 6, pp 71–79

Johansson S, Engqvist J, Tryding J et al (2021) 3d strain field evolution and failure mechanisms in anisotropic paperboard. Exp Mech 61(3):581–608. https://doi.org/10.1007/s11340-020-00681-7

Kanatani KI (1984) Distribution of directional data and fabric tensors. Int J Eng Sci 22(2):149–164. https://doi.org/10.1016/0020-7225(84)90090-9

Kloppenburg G, Li X, Dinkelmann A, et al (2023a) Identifying microstructural properties of paper. PAMM https://doi.org/10.1002/pamm.202300251

Kloppenburg G, Walther E, Holthusen H, et al (2023b) Using numerical homogenization to determine the representative volume element size of paper. PAMM https://doi.org/10.1002/pamm.202200226

Köbler J, Schneider M, Ospald F et al (2018) Fiber orientation interpolation for the multiscale analysis of short fiber

reinforced composite parts. Comput Mech 61(6):729–750. https://doi.org/10.1007/s00466-017-1478-0

Kulachenko A, Gradin P, Uesaka T (2007) Basic mechanisms of fluting formation and retention in paper. Mech Mater 39(7):643–663. https://doi.org/10.1016/j.mechmat.2006.10.002

Lahti J, Dauer M, Keller DS et al (2020) Identifying the weak spots in packaging paper: local variations in grammage, fiber orientation and density and the resulting local strain and failure under load. Cellulose 27(17):10327–10343. https://doi.org/10.1007/s10570-020-03493-z

Lavrykov SA, Ramarao B, Lyne OL (2004) The planar transient hygroexpansion of copy paper: experiments and analysis. Nordic Pulp Paper Res J 19(2):183–190. https://doi.org/10.3183/npprj-2004-19-02-p183-190

Leppänen T (2007) Effect of fiber orientation on cockling of paper (kuituorientaation vaikutus paperin kupruiluun). PhD thesis, University of Kuopio

Li Y, Stapleton SE, Reese S et al (2016) Anisotropic elastic-plastic deformation of paper: In-plane model. Int J Solids Struct 100–101:286–296. https://doi.org/10.1016/j.ijsolstr.2016.08.024

Li Y, Yu Z, Reese S, et al (2018) Evaluation of the out-of-plane response of fiber networks with a representative volume element model. Tappi J 17(6):329–339. https://doi.org/10.32964/TJ17.06.329

Lin B, Auernhammer J, Schäfer JL et al (2021) Humidity influence on mechanics of paper materials: joint numerical and experimental study on fiber and fiber network scale. Cellulose 29(2):1129–1148. https://doi.org/10.1007/s10570-021-04355-y

Lindner M (2017) Factors affecting the hygroexpansion of paper. J Mater Sci 53(1):1–26. https://doi.org/10.1007/s10853-017-1358-1

Lipponen P, Leppänen T, Kouko J et al (2008) Elasto-plastic approach for paper cockling phenomenon: on the importance of moisture gradient. Int J Solids Struct 45(11–12):3596–3609. https://doi.org/10.1016/j.ijsolstr.2008.02.017

Martin JJ, Riederer MS, Krebs MD et al (2015) Understanding and overcoming shear alignment of fibers during extrusion. Soft Matter 11(2):400–405. https://doi.org/10.1039/c4sm02108h

Marulier C, Dumont PJJ, Orgéas L et al (2012) Towards 3d analysis of pulp fibre networks at the fibre and bond levels. Nordic Pulp Paper Res J 27(2):245–255. https://doi.org/10.3183/NPPRJ-2012-27-02-p245-255

Marulier C, Dumont PJJ, Orgéas L et al (2015) 3d analysis of paper microstructures at the scale of fibres and bonds. Cellulose 22(3):1517–1539. https://doi.org/10.1007/s10570-015-0610-6

Mendes AdO, Fiadeiro P, Costa A et al (2015) Laser scanning for assessment of the fiber anisotropy and orientation in the surfaces and bulk of the paper. Nordic Pulp Paper Res J 30(2):308–318. https://doi.org/10.3183/npprj-2015-30-02-p308-318

Miao C, Hamad WY (2013) Cellulose reinforced polymer composites and nanocomposites: a critical review. Cellulose 20(5):2221–2262. https://doi.org/10.1007/s10570-013-0007-3

Motloung MP, Ojijo V, Bandyopadhyay J et al (2019) Cellulose nanostructure-based biodegradable nanocomposite foams: a brief overview on the recent advancements and perspectives. Polymers 11(8):1270. https://doi.org/10.3390/polym11081270

Müller V, Brylka B, Dillenberger F et al (2015) Homogenization of elastic properties of short-fiber reinforced composites based on measured microstructure data. J Compos Mater 50(3):297–312. https://doi.org/10.1177/0021998315574314

Neumann M, Machado Charry E, Baikova E et al (2021) Capturing centimeter-scale local variations in paper pore space via µ-ct: a benchmark study using calendered paper. Microscopy Microanal 27(6):1305–1315. https://doi.org/10.1017/S1431927621012563

Niskanen K (2008) Papermaking science and technology: paper physics. Forest Products Engineers Finland, Helsinki

Niskanen K, Sadowski J (1989) Evaluation of some fibre orientation measurements. J Pulp Paper Sci 15(6):J220–J224

Niskanen K, Sadowski J (1990) Fiber orientation in paper by light diffraction. J Appl Polym Sci 39(2):483–486. https://doi.org/10.1002/app.1990.070390223

Nygårds M (2022) Relating papermaking process parameters to properties of paperboard with special attention to through-thickness design. MRS Adv 7(31):789–798. https://doi.org/10.1557/s43580-022-00282-7

Orgéas L, Dumont PJJ, Martoïa F et al (2021) On the role of fibre bonds on the elasticity of low-density papers: a micro-mechanical approach. Cellulose 28(15):9919–9941. https://doi.org/10.1007/s10570-021-04098-w

Perkins R, Mark R (1981) Some new concepts of the relation between fibre orientation, fibre geometry, and mechanical properties. In: The role of fundamental research in papermaking, Trans. of the VIIth Fund. Res. Symp. Cambridge, 1981, p 479-525, https://doi.org/10.15376/frc.1981.1.479

Prud'homme RE, Hien N, Noah J et al (1975) Determination of fiber orientation of cellulosic samples by X-ray diffraction. J Appl Polym Sci 19(9):2609–2620

Rolland du Roscoat S, Decain M, Thibault X et al (2007) Estimation of microstructural properties from synchrotron X-ray microtomography and determination of the rev in paper materials. Acta Mater 55(8):2841–2850. https://doi.org/10.1016/j.actamat.2006.11.050

Rolland du Roscoat S, Bloch JF, Caulet P (2012) A method to quantify the 3d microstructure of fibrous materials containing mineral fillers using x-ray microtomography: application to paper materials. J Mater Sci 47(18):6517–6521. https://doi.org/10.1007/s10853-012-6575-z

Sampson W (2001) The structural characterisation of fibre networks in papermaking processes—a review. In: Proceedings of the transactions of 12th fundamental resource symposium, Oxford, pp 1205–1288, https://doi.org/10.15376/frc.2001.2.1205

Schaffrath HJ, Tillmann O (2013) Testing of fibers. Suspensions, and paper and board grades, John Wiley & Sons Ltd, chap 29:1059–1086. https://doi.org/10.1002/9783527652495.ch29

Schulgasser K (1985) Fibre orientation in machine-made paper. J Mater Sci 20(3):859–866. https://doi.org/10.1007/BF00585727

Simon JW (2021) A review of recent trends and challenges in computational modeling of paper and paperboard at different scales. Arch Comput Methods Eng 28(4):2409–2428. https://doi.org/10.1007/s11831-020-09460-y

Titus M (1994) Ultrasonic technology: measurements of paper orientation and elastic properties. Tappi J 77(1):127–130

Uesaka T (1994) General formula for hygroexpansion of paper. J Mater Sci 29:2373–2377

Urstöger G, Kulachenko A, Schennach R et al (2020) Microstructure and mechanical properties of free and restrained dried paper: a comprehensive investigation. Cellulose 27(15):8567–8583. https://doi.org/10.1007/s10570-020-03367-4

Viguié J, Latil P, Orgéas L et al (2013) Finding fibres and their contacts within 3d images of disordered fibrous media. Compos Sci Technol 89:202–210. https://doi.org/10.1016/j.compscitech.2013.09.023

Wahlström T (2009) Prediction of fibre orientation and stiffness distributions in paper—an engineering approach. Adv Pulp Paper Res https://doi.org/10.15376/frc.2009.2.1039

Wahlström T (2013) Predictions of md and cd tensile property profiles. Adv Pulp Paper Res https://doi.org/10.15376/frc.2013.2.673

Wallmeier M, Barbier C, Beckmann F et al (2021) Phenomenological analysis of constrained in-plane compression of paperboard using micro-computed tomography imaging.
Nordic Pulp Paper Res J 36(3):491–502. https://doi.org/10.1515/npprj-2020-0092